Studies of cosmic-ray electrons with the H.E.S.S. experiment using an advanced reconstruction technique

Diplomarbeit
von
Stephanie Häffner

Erlangen Centre for Astroparticle Physics
Physikalisches Institut
Lehrstuhl für Physik
Friedrich-Alexander-Universität Erlangen-Nürnberg

1. Gutachter: Prof. Ch. Stegmann
2. Gutachter: Prof. U. Katz

15. Juni 2010

Abstract

The high-energy cosmic-ray electron spectrum has been measured by H.E.S.S., a stereoscopic imaging atmospheric Cherenkov telescope array situated in the Khomas highland in Namibia, in the energy range between 360 GeV and 14 TeV. This work studies the electron reconstruction using an advanced reconstruction technique (model analysis), that reaches a better sensitivity to electromagnetic air showers than the standard Hillas reconstruction and provides the depth of first interaction as additional output parameter. A clear electron/hadron separation with good signal efficiency can be achieved using the Boosted Decision Tree method. The model analysis allows a good electron energy reconstruction above 300 GeV, but in order to further decrease the energy threshold for an electron analysis, the data have to meet strict quality requirements and constraints on event selection. Although the model analysis provides, apart from the depth of shower maximum, the depth of first interaction as sensitive parameter to differences in shower evolution between electron and γ-ray induced air showers, an electron/γ-ray separation with good signal efficiency on an event-by-event basis with the strategy applied in this work is not possible.

Zusammenfassung

Das Spektrum hoch-energetischer kosmischer Elektronen wurde bereits mit H.E.S.S., einem System aus abbildenden atmosphaerischen Cherenkov-Teleskopen, das sich im Khomas Hochland in Namibia befindet, im Energiebereich zwischen 360 GeV und 14 TeV gemessen. Diese Arbeit untersucht die Elektronenrekonstruktion mit einer fortgeschrittenen Rekonstruktionstechnik (Model-Analyse), die eine bessere Sensitivität gegenüber elektromagnetischen Luftschauern als die Standard-Hillas-Rekonstruktion aufweist und außerdem als Schauer-Parameter die Höhe der ersten Wechselwirkung bereitstellt. Eine klare Elektron-Hadron-Trennung mit guter Signaleffizienz wird mittels der Boosted Decision Tree Methode erreicht. Die Model-Analyse erlaubt eine gute Energierekonstruktion für Elektronen oberhalb von 300 GeV, aber um die Energieschwelle weiter zu senken, müssen strikte Kriterien bei der Ereignis- und Beobachtungsauswahl erfüllt werden. Obwohl die Model Analyse mit der Höhe der ersten Wechselwirkung neben der Höhe der maximalen Schauerausbreitung einen zweiten Parameter bietet, der sensitiv auf Unterschiede in der Schauerentwicklung bei elektron- und photoninduzierten Luftschauern ist, kann keine Elektron-Gamma-Strahlungs-Trennung mit den hier angewandten Strategien mit guter Signaleffizienz erzielt werden.

Contents

List of Figures

Chapter 1

Introduction

Cosmic rays were discovered by Victor Hess in the 1910s with balloon experiments, explaining the rising radiation at increasing altitudes in the atmosphere. The main components of cosmic rays are protons and heavier nuclei, but they also consist of electrons and photons. The hadronic component is very well measured in a wide energy range between 10^9 eV and 10^{21} eV. The cosmic-ray electrons were only measured above a few GeV up to 2 TeV by balloon and satellite-borne experiments. In 2008 H.E.S.S. presented an energy spectrum of high-energy cosmic-ray electrons up to 14 TeV [1], which was the first measurement of those electrons with an imaging atmospheric Cherenkov telescope array(IACT).

Usually, IACTs are used as observation instruments for ground based γ-ray astronomy. However, both high-energy electrons and γ-rays initiate electromagnetic air showers, which are observable with IACTs. H.E.S.S. has been operating with four telescopes since 2003 and the systematics of the instrument are very well understood. Even very faint sources, such as SN 1006 [2] with a γ-ray flux about 1% of the Crab flux, are detected with an advanced γ-ray reconstruction technique [3].

This reconstruction technique (model analysis) provides a better sensitivity to electromagnetic air showers than the Hillas standard reconstruction and also yields the depth of first interaction as a reconstruction output parameter. Electron and γ-ray initiated air showers are similar, but electrons generally interact immediately entering the Earth's atmosphere, whereas γ-rays propagate on average deeper into the atmosphere. Thus, the parameter of the depth of first interaction motivates an investigation of electron/γ-ray separation.

This work studies cosmic-ray electrons using the model analysis as well as a possible electron/γ-ray separation. It starts with an overview about high-energy electrons in Chapter 2. The H.E.S.S. measurement of the high-energy cosmic-ray electron spectrum and other cosmic-ray electron measurements are presented. Potential sources and acceleration processes are discussed.

Chapter 3 introduces the H.E.S.S. experiment and explains the physics of air showers, as well as the observation principle of IACTs.

The identification of electrons is presented in Chapter 4, starting with the reconstruction and explaining the electron/hadron separation with the method of Boosted Decision Trees. The application to data and a successful electron/hadron separation are presented. The estimation of remaining background is also described.

Chapter 5 summarises steps needed to obtain a high-energy cosmic-ray electron spectrum with emphasis on effective collection area and energy threshold.

Motivated by the reconstruction output parameter the depth of first interaction, Chapter 6 presents a study of electron/γ-ray separation with the method of Boosted Decision Trees.

A conclusion of this work and an outlook are given in Chapter 7.

Chapter 2

High-energy cosmic-ray electrons

Cosmic-ray electrons have been measured with H.E.S.S. and other experiments between 1 GeV and 14 TeV. This Chapter gives an overview about the existing measurements of the spectrum of high-energy cosmic-ray electrons in Section 2.1, presents the most important energy loss processes during electron propagation (Section 2.2), gives an overview of potential nearby sources and explains how contributors to the cosmic-ray electron flux in the solar system could be identified (Section 2.3). Also the basic principles of particle acceleration in supernovae and pulsar magnetospheres are described in Section 2.4.
Throughout this work the term "electron" refers to both particle and antiparticle unless specified otherwise, because the H.E.S.S. measurement cannot determine the electric charges.

2.1 The spectrum of high-energy cosmic-ray electrons

The energy spectrum of high-energy cosmic-ray electrons has been measured between 1 GeV and 2 TeV with balloon and satellite-borne experiments, but beyond 2 TeV the flux becomes too low for these experiments. In 2008 H.E.S.S. presented the first ground-based measurement of high-energy cosmic-ray electrons in the energy range between 600 GeV and 14 TeV with an imaging atmospheric Cherenkov telescope Array[1]. Figure 2.1 shows the H.E.S.S. measurement extended to lower energies [4] together with measurements by ATIC [5], PPB-BETS [6], Kobayashi et al. [7] and Fermi-LAT [8]. The BETS and ATIC detectors use imaging calorimeters measuring the longitudinal and lateral shower development. Kobayashi et al. [7] use emulsion chambers to observe the shower and Fermi-LAT measures electrons with a siliconstrip tracker, calorimeter and anticoincidence plastic scintillator detector. The H.E.S.S. experiment is ground based and reconstructs the energy and direction of the primary particle from the Cherenkov light emitted by the air shower of the secondary particles.

In the energy range between approximately 10 GeV and 1 TeV the spectrum of cosmic-ray electrons can be described by a power law $dN/dE \propto E^{-\Gamma}$ with a spectral index of $\Gamma = 3.3$. The ATIC experiment stirred interest with a "bump", the so called *ATIC-Peak*, in the spectrum between 300 and 800 GeV, which led to intensified discussion of a potential dark matter signature (see for example [9] and references therein). But neither the Fermi-LAT data nor the H.E.S.S. low-energy measurement confirm this feature.

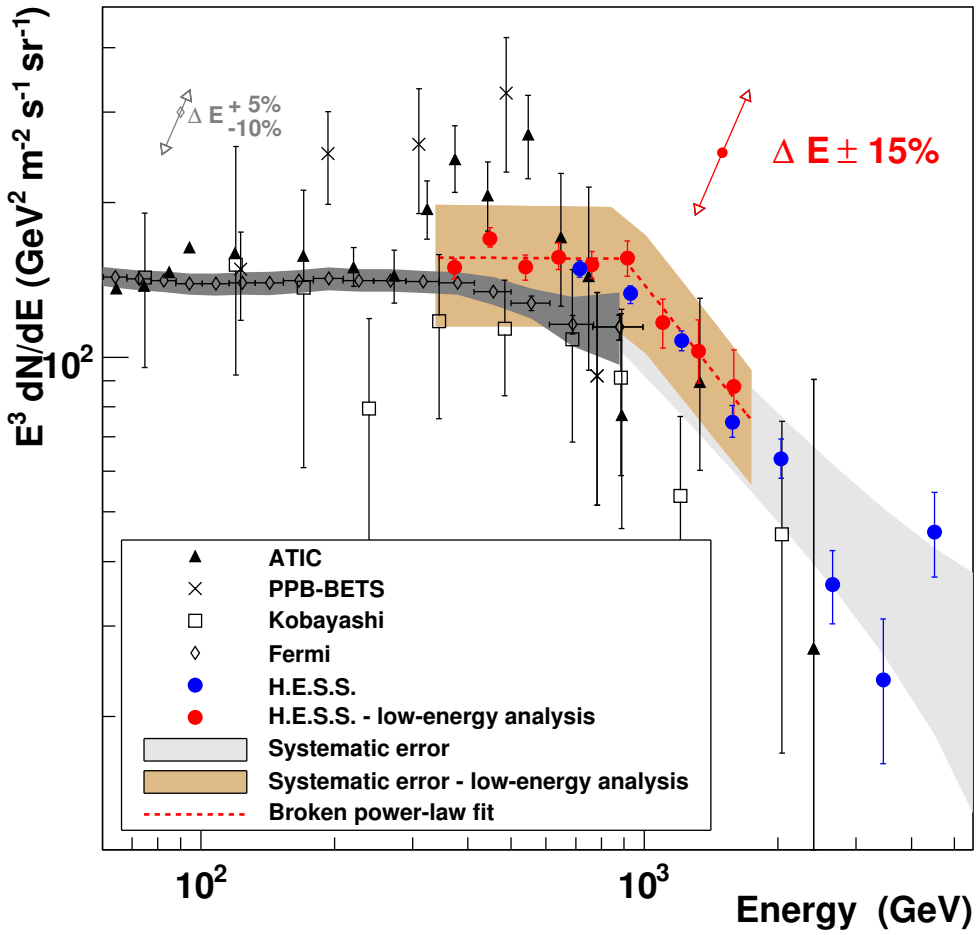

Figure 2.1: The energy spectrum of high-energy cosmic-ray electrons, depicted as $E^3\ dN/dE$, as measured by ATIC [5], PPB-BETS [6], Kobayashi et al. [7], Fermi-LAT [8] (the dark grey band indicates the Fermi-LAT systematic uncertainty, the grey arrow a $+5\%/-10\%$ the uncertainty of the Fermi-LAT energy scale) and H.E.S.S. [1]. Blue points show the 2008 H.E.S.S. measurement, red points the H.E.S.S. low-energy measurement in 2009 [4]. The shaded bands represent the systematic uncertainties from hadronic and atmospheric models and the red arrow indicates an energy uncertainty of 15%. This plot is taken from [4].

The H.E.S.S. data [4] can be described by a broken power law

$$\frac{dN}{dE} = k \cdot \left(\frac{E}{E_b}\right)^{-\Gamma_1} \cdot \left(1 + \left(\frac{E}{E_b}\right)^{\frac{1}{\alpha}}\right)^{-(\Gamma_2-\Gamma_1)\alpha} \tag{2.1}$$

with a normalisation $k = (1.5 \pm 0.1) \cdot 10^{-4}\,\mathrm{TeV}^{-1}\mathrm{m}^{-2}\mathrm{sr}^{-1}\mathrm{s}^{-1}$ and a break energy $E_b = 0.9 \pm 0.1\,\mathrm{TeV}$. The spectral indices have the value $\Gamma_1 = 3.0 \pm 0.1$ and $\Gamma_2 = 4.1 \pm 0.3$, respectively. The sharpness of the transition between both power laws is given by $\alpha < 0.3$.

For the H.E.S.S. measurement of the high-energy cosmic-ray electron energy spectrum data from extragalactic observations excluding potential γ-ray sources were used and the background was estimated by models with proton Monte Carlo simulations.

The systematic uncertainties in the flux normalisation are indicated in figure 2.1 with shaded bands and amount up to 30%. These arise from uncertainties in the modelling of hadronic interactions and atmospheric fluctuations. The uncertainties of the hadronic interactions were derived from comparison of spectra that were obtained using the SIBYLL and QGSGET-II hadronic interaction models. The atmospheric modelling uncertainties were estimated by taking two independent data sets from summer and autumn 2004. In the standard H.E.S.S. Hillas reconstruction [10] the energy scale has an uncertainty of 15%, which is indicated by an arrow in figure 2.1.

An advanced reconstruction technique of electromagnetic air showers [3] (see also Section 4.1) can provide an energy resolution better than 15% with less than 10% in the central energy range between 500 GeV and more than 10 TeV. It is also more sensitive to electromagnetic air showers at low energies than the standard Hillas reconstruction. This could lead to a lower energy threshold in the measurement of high-energy cosmic-ray electrons (see Section 5.3).

2.2 Propagation and energy losses of electrons

The energy losses for the cosmic-ray electron and hadron components are different. Electrons lose much more energy during propagation through matter, radiation fields and magnetic fields. Therefore the resulting electron spectrum is significantly steeper than the spectrum of the hadronic cosmic-ray component which can be described by a power law with a spectral index $\Gamma = 2.7$. This Section briefly summarises the main energy losses for high-energy electrons (detailed discussion e.g. in [7] and [11]).

Cosmic-ray electrons mainly lose energy via ionisation, synchrotron radiation and inverse Compton scattering. These losses are described as:

$$-\frac{dE}{dt} = A_1 \ln\left(\frac{E}{m_e c^2} + 19.8\right) + A_2 E + A_3 E^2. \tag{2.2}$$

The term with coefficient A_1 describes ionisation losses and depends only weakly on energy. These losses decrease logarithmically with energy and dominate at electron energies of a few MeV. Bremsstrahlung and adiabatic energy losses are represented in the A_2 term and are proportional to the electron energy. The last term with A_3 describes the energy losses due to synchrotron radiation and inverse Compton scattering.

The resulting electron spectrum can differ from the initial electron spectrum depending on which loss process is dominating:

- If ionisation losses dominate, the energy spectrum is flattened by one power of E,

- if bremsstrahlung or adiabatic losses dominate, the spectrum remains unchanged,
- if inverse Compton scattering or synchrotron losses dominate, the spectrum is steepened by one power of E.

The dominant energy loss processes for high-energy electrons above 10 GeV are inverse Compton scattering and synchrotron radiation and hence equation 2.2 can be reduced to the quadratic term:

$$-\frac{dE}{dt} = A_3 E^2 \tag{2.3}$$

with

$$A_3 = \frac{4\sigma c}{3(m_e c^2)^2}\left(\frac{B^2}{8\pi} + w_{ph}\right). \tag{2.4}$$

Here E is the electron energy, m_e the electron mass, c the speed of light, B the magnetic field strength in the Galaxy, w_{ph} is the energy density of interstellar photons and σ the cross section for Thomson scattering. For very high-energy electrons the Klein-Nishina cross section has to be used instead of the Thomson cross section. An adequate value of the local magnetic field perpendicular to the electron velocity is $B_\perp = 5\,\mu$G. The interstellar radiation field with which electrons interact is composed of the cosmic microwave background (CMB), reemitted radiation from dust grains and stellar radiation. Interactions with the CMB with an energy density of $0.26\,\mathrm{eVcm}^{-3}$ are dominant for TeV electrons.

According to equation 2.3 electrons lose in average almost all their energy after a time $T = 1/bE$ and the mean electron lifetime was calculated as $T \approx 2.5 \cdot 10^5$ yr$/(E$ [TeV]) by the authors of [7]. Thus, depending on the diffusion coefficient, electrons at 1 TeV propagate only $0.6 - 0.9$ kpc, which means that any source that produces electrons detectable on Earth must be very nearby in galactic relations.

2.3 Potential sources of cosmic-ray electrons

Depending on their origin, cosmic-ray electrons can be divided into primary and secondary electrons. Primary electrons are emitted by astrophysical objects like shock fronts in supernova remnants (SNR), pulsar magnetospheres or pulsar wind nebulae (PWN). These sources of primary electrons are indicated by radio and X-ray observations. Also some VHE γ-ray observations, for example of the PWN Vela X, indicate a more likely lepton origin (for detailed discussion of H.E.S.S. observations of PWN see e.g. [12]). Various dark matter scenarios were also discussed recently concerning the ATIC-Peak in the electron spectrum between 300 GeV and 800 GeV (see [9] and references therein).

Secondary cosmic-ray electrons originate in interactions of high-energy cosmic-rays with the interstellar medium:

$$\begin{array}{ll} p + p \rightarrow \pi^{\pm} X, & \\ \pi^+ \rightarrow \mu^+ \nu_\mu, & \pi^- \rightarrow \mu^- \bar{\nu}_\mu, \\ \mu^+ \rightarrow e^+ \nu_e \bar{\nu}_\mu, & \mu^- \rightarrow e^- \bar{\nu}_e \nu_\mu. \end{array} \tag{2.5}$$

For a discussion of the secondary electron contributions see for example [13].

As indicated in Section 2.2, the limited mean lifetime of high-energy electrons leads to typical propagation distances below 1 kpc. This strongly reduces the number of potential sources within our Galaxy.

Table 2.1: List of SNRs and pulsars, that are younger than $5 \cdot 10^5$ years and within 1 kpc distance to Earth.

source	distance [kpc]	age [yr]
SNRs:		
RXJ0852.0-662/Vela Jr.	0.33	660
SN 185	0.95	$1.8 \cdot 10^3$
S147	0.80	$4.6 \cdot 10^3$
G114.3+0.3	0.7	$7.7 \cdot 10^3$
HB 21	0.80	$1.9 \cdot 10^4$
G65.3+5.7	0.80	$2.0 \cdot 10^4$
Cygnus Loop	0.44	$2.0 \cdot 10^4$
Vela	0.30	$1.1 \cdot 10^4$
Monogem Ring	0.30	$8.6 \cdot 10^4$
Loop I	0.17	$2.0 \cdot 10^5$
Geminga	0.4	$3.4 \cdot 10^5$
Pulsars:		
Vela Pulsar	0.29	$1.13 \cdot 10^4$
Monogem	0.29	$1.11 \cdot 10^5$
J1825-0935	1.00	$2.33 \cdot 10^5$

Also the age of supernova remnants limits the variety of potential sources. Shock acceleration theory suggests that electrons are released from supernova remnants in the termination of the shock. The shock velocity drops down within a timescale of approximately 10^5 years. The most promising young and nearby SNRs and pulsars that could contribute to the electron flux in the solar system are listed in table 2.1 ([7, 14]).

Identifying nearby sources

Kobayashi et al. [7] calculated the cosmic-ray electron spectrum in the solar system separating the contributions of distant and nearby sources to the total electron flux. They showed that nearby sources could leave identifiable structures in the high-energy spectrum of cosmic-ray electrons. Figure 2.2 shows an example of the calculated energy spectrum. Depending on the diffusion coefficient, the release time from the SNR and the initial electron spectrum. Vela, Cygnus Loop and Monogem could leave unique signatures in the spectrum above 1 TeV. However, the H.E.S.S. measurement (see figure 2.1) shows no such feature and hence some scenarios of a strong local source are excluded [4].

Apart from the above mentioned features in the energy spectrum of high-energy cosmic electrons, an anisotropy of the electron flux might help to identify local sources. If there are local sources an anisotropy in the electron flux towards and away from the sources would be expected. For each source i an anisotropy parameter Δ_i is defined [15, 16]:

$$\Delta_i \equiv \frac{I_{max} - I_{min}}{I_{max} + I_{min}} = \frac{3D}{c} \frac{\nabla N_i}{N_i} = \frac{3r_i}{2ct_i}. \tag{2.6}$$

I_{max} and I_{min} are the minimum and maximum intensity of the flux in all directions, N_i is the contribution to the local cosmic-ray electron intensity by a source i at a distance r_i and an age t_i. The expected anisotropy of electrons for Vela is 13% [7]. However, the uncertainties of the

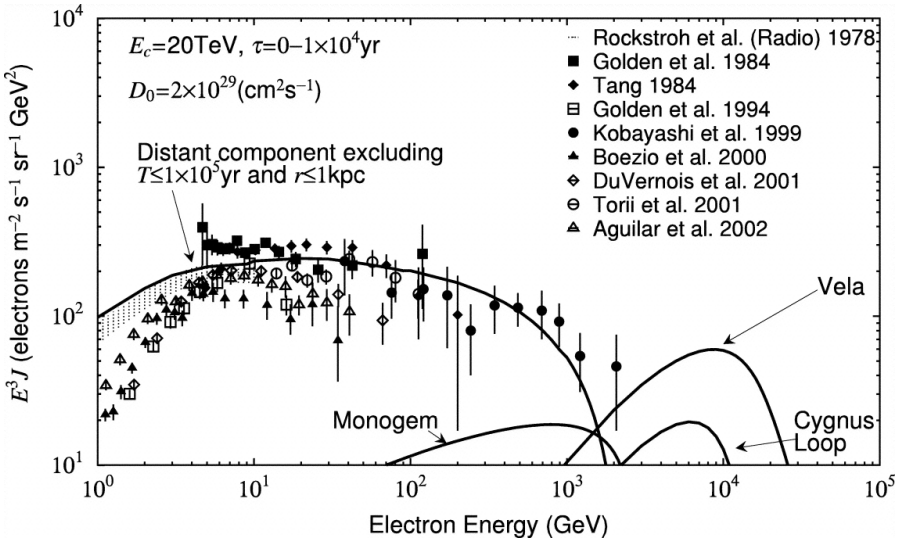

Figure 2.2: Example for a calculated energy spectrum of electrons (taken from [7]). The shape of the spectrum strongly depends on the diffusion coefficients D_0, release time τ and cut-off energy E_c.

already measured high-energy cosmic-ray electron spectrum with H.E.S.S. above 400 GeV are too high to observe such an anisotropy [14].

Dark Matter[1]

As already mentioned, the ATIC peak in the electron spectrum stirred interest, which resulted in an intensified discussion of an potential dark matter (DM) or pulsar related origin. Various DM scenarios are under debate (see [9], especially references within), but a large class of the annihilating/decaying DM models predict an electron flux in form of an power law with a universal index $n = 2$ at energies below M_{DM}, the DM mass. This results from the domination of the energy loss proportional to A_3E^2 below M_{DM}.
The predicted flux, in contrary to pulsar models, for one DM model depends only on a few parameters:
the energy loss A_3E^2, the number density of electrons produced per annihilation/decay event dN/dE, the dark matter number density n_χ, the thermally averaged annihilation cross section $\langle\sigma v\rangle$ and the DM mass M_{DM}.

Thus, if the energy loss is well understood and the DM number density is constrained by cosmological models and observations, the flux for one DM model providing a certain number of produced electrons has only two free parameters: M_{DM} and $\langle\sigma v\rangle$. The mass is fixed by the cut-off energy and $\langle\sigma v\rangle$ is determined by the flux normalisation.

With observations available at the moment, no distinction between a pulsar or DM dominated electron flux is possible.

[1]The information in this short discussion is taken from [9].

2.4 Acceleration processes

As already mentioned SNRs, pulsars and PWNs are discussed as potential sources of high-energy electrons and observations in different wavelengths confirm the existence of high-energy electrons in these objects. PWNs with low magnetic fields are observable in very high-energy (VHE) γ-ray astronomy due to inverse Compton scattering if the electron energy is not limited by synchrotron radiation [12]. This section gives an overview about the basic principles of different acceleration processes, detailed descriptions are still under debate. For an in-depth discussion of these acceleration processes see for example [11] and [17].

Shock acceleration in supernova explosions

The stellar evolution of a high-mass star ends with a supernova explosion. The iron core of the star collapses and the outer layers of the star are ejected. These layers expand with very high velocities ($\approx 1000 - 2000\,\mathrm{km/s}$) into the interstellar medium (ISM) and form a shock front because of their supersonic velocity. The expansion continues until the shock wave sweeps up enough mass from the ISM and slows down (Sedov-Taylor phase). During these shock phases electrons are accelerated on the shock fronts. In later stages the temperature of the shock drops below $10^6\,\mathrm{K}$ and the free electrons recombine with heavier ions.

A first approach to explain particle acceleration to high energies was suggested by E. Fermi in 1949 [18], but he considered only stochastically moving "magnetic mirrors". In this approach the energy gain is proportional to the squared ratio of the speed of these magnetic mirrors v and the speed of light c. This mechanism, which is known today as *Second Order Fermi Acceleration*, can not explain particle acceleration to relativistic energies, because the random velocities of interstellar clouds in the Galaxy (which might represent such magnetic mirrors) are very small, $v/c \leq 10^{-4}$. Furthermore due to the mean free path of cosmic rays the number of collision per year would be very small, leading to a very slow gain of energy by the particles. There are also some injection problems, when taking into account the energy loss processes during acceleration.

In the 1970s the process of diffusive shock acceleration was developed [19, 20, 21, 22], which describes an energy gain proportional to v/c.

The region of interaction between the SNR and the ISM consists of a forward shock, where ambient gas is compressed and heated, and a reverse shock, where ejecta are accelerated. Both shocks are separated by a contact discontinuity with local instabilities. During the expansion of the shock fronts into the interstellar medium with a shock velocity v, particles with sufficient energy can cross the shock front and get accelerated. In front of and behind both shock fronts particles scatter off magnetic inhomogeneities produced by shock turbulence and streaming instabilities of the relativistic particles. These scatterings lead to an isotropic velocity distribution with respect to the frame of reference where the fluid is at rest. The particles are accelerated due to the momentum of the crossed shock front. This is a symmetric process and the particles gain energy proportional to v/c with each forward or backward crossing of the shock front. This acceleration process has been termed *First Order Fermi Acceleration* in order to distinguish it from the afore mentioned second-order process.

Acceleration in pulsar magnetospheres and PWNs

Particles can not only be accelerated during the shock expansion of a supernova, but also in the magnetosphere of pulsars. Pulsars are fast-rotating neutron stars with periods P of a few seconds to milliseconds. They are formed at the end of stellar evolution if the mass of the core of the progenitor star is above approximately $1.4\,\mathrm{M}_\odot$ (Chandrasekhar limit) and below about $3\,\mathrm{M}_\odot$ (Tolman–Oppenheimer–Volkoff limit). Progenitor stars with lower masses end their life as white dwarfs, if the mass is higher than this range, a black hole is formed. Pulsars possess extremely high magnetic fields with $10^{10}\,\mathrm{G}$ to $10^{13}\,\mathrm{G}$. Strong electric fields arise from the fast rotation and highly compressed magnetic fields of the pulsar which can accelerate particles to high energies.

A so-called magnetosphere consisting of particles pulled out of the pulsar surface by the electric field surrounds the pulsar and corotates with it. The radius of the magnetosphere is limited by the particles' inertia and the speed of light c. The distance where the corotation speed of the particles in the magnetosphere becomes equal to c defines a so-called light cylinder with the radius $R_c = c/\Omega$ with $\Omega = 2\pi/P$. Within this radius the magnetic field lines are closed and the particles that gyrate around these field lines are captured. Outside the light cylinder the magnetic field lines are open and the accelerated particles can escape. The electric field component $E_\parallel$ parallel to the magnetic field lines must not vanish in order for particle acceleration to occur. Usually, screening effects of charged particles within the magnetosphere lead to vanishing $E_\parallel$.

In the so-called *polar cap* models the acceleration takes place, as the name already implies, in charge-free zones near the polar caps of the pulsar. The *outer gap* models, on the other hand, describe vacuum gaps along null-charge surfaces, which separate regions of the opposite sign of the corotation charge. In both models particles are accelerated and can escape along open field lines.

In regions with $E_\parallel \neq 0$ electromagnetic cascades are produced. γ-rays emitted by synchrotron radiation interact with the strong magnetic fields and produce e^+e^- pairs. The secondary particles are again accelerated, radiate synchrotron light and thereby initiate a cascade. Particles leaving the magnetosphere and the light cylinder form a so-called pulsar wind nebula (PWN) and escaping electrons have small velocities. In the outer regions the PWN interacts with the expanding supernova shell and a termination shock is formed. Here particles can also get accelerated to high energies like in the expanding supernova shock fronts.

Chapter 3

H.E.S.S. - an imaging atmospheric Cherenkov telescope array

The H.E.S.S. experiment is an imaging atmospheric Cherenkov telescope (IACT) array that observes very-high energetic photons in the energy range between 100 GeV and 100 TeV[1] indirectly via the Cherenkov radiation emitted by the secondary particles of the induced air shower. The evolution and properties of air showers are described in Section 3.1. The emission of Cherenkov light and the basic principles of IACTs are explained in Section 3.2. An overview of the H.E.S.S. experiment is given in Section 3.3.

3.1 Air showers

Since they are absorbed in the Earth's atmosphere, high-energy γ-rays can not be observed directly on the ground. To avoid this problem, X-ray astronomers use satellite-borne experiments for direct photon detection, but the flux in the TeV energy range is too low in matter of the limited collection areas available on spacecraft. Therefore, ground-based Very High Energy (VHE) γ-ray astronomy uses the Earth's atmosphere as a "calorimeter" and observes secondary particles produced in the interactions.

3.1.1 Heitler model of an air shower

Air showers are produced when high-energy cosmic rays hit air molecules in the atmosphere and initiate a cascade of secondary particles. If, for example, the primary particle is a cosmic-ray photon, it will interact with the Coulomb field of an atom high up in the atmosphere and produce an electron-positron pair. The secondary particles generate γ-rays via bremsstrahlung, which in turn yield new electron-positron pairs: an electromagnetic cascade is initiated. With each new generation the energy of the particles decreases and the cross sections for the different processes change with particle energy. The emission of bremsstrahlung (and thus the subsequent production of more electron positron pairs) is suppressed once ionisation and excitation become the predominant energy loss mechanisms of the electrons. This occurs when the energy of the shower particles drops below a so-called critical energy E_c, at which point the production of new shower particles and hence the evolution of the cascade is stopped.

[1] The upper energy limit depends on the flux of the observed source.

In a very similar manner, electromagnetic air showers can also be initiated by cosmic-ray electrons, with the first interaction process being the emission of a photon by bremsstrahlung instead of the pair production in the case of the primary particle being a photon.

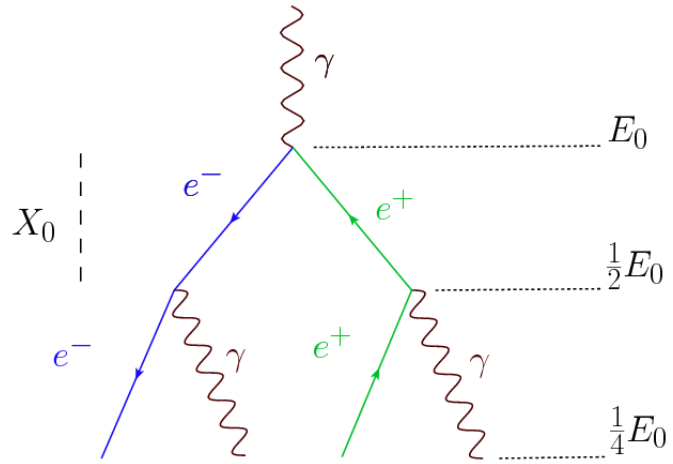

Figure 3.1: Heitler model for the evolution of an electromagnetic air shower.

A simple description of an electromagnetic air shower was introduced by W. Heitler in 1954 [23]. This model considers only bremsstrahlung and pair production for particle creation and is illustrated in figure 3.1. Here it is assumed that in each generation the energy of all secondary particles is equipartioned. The shower consists of $N(x) = 2^{(x/X_0)}$ particles after a distance x and $n = x/X_0$ branchings. X_0 is the radiation length [2] and has the value $X_0 = 3.72$ g cm^{-2} in air. Each of the $N(x)$ particles has on average an energy $E(x) = E_0 \cdot 2^{(-x/X_0)}$. Here, E_0 denotes the energy of the incident primary particle.

The depth of the shower maximum in the atmosphere X_{max} can be estimated as

$$X_{max} = \frac{\ln(E_0/E_c)}{\ln 2} \cdot X_0. \tag{3.1}$$

E_c is the critical energy (≈ 80 MeV in air) where the shower development stops because the ionisation of atmosphere's molecules is dominant over the bremsstrahlung and pair creation processes. If X_{max} is known the number of particles at the shower maximum N_{max} can be calculated as

$$N_{max} = 2^{X_{max}/X_0} = \frac{E_0}{E_c}. \tag{3.2}$$

This simple model predicts a proportionality between the maximal number of shower particles and the energy E_0 of the primary particle as well as an increasing depth of the shower maximum that depends logarithmically on the primary energy E_0. Realistic shower simulations that also take into account energy loss processes during shower formation and other higher order interaction processes confirm these properties. For a 1 TeV γ-ray the shower maximum is typically located at a height of ≈ 10 km above sea level.

In the previous discussion only electron- or photon-induced air showers were considered. However, the majority of cosmic rays consists of hadronic particles (predominantly protons or very light atomic nuclei). These can also induce air showers, which are generally referred to as "hadronic air

[2] The radiation length X_0 is defined as the mean distance over which a high-energy electron loses all but $1/e$ of its energy via bremsstrahlung and also 7/9 of the mean free path for pair production by a high energy photon [24]. But in this simple model the assumption is made, that both lengths are equal for relativistic particles.

showers". An important difference between hadronic and electromagnetic cascades is the admixture of hadronic interactions which characterises the former. The essential differences between electromagnetic and hadronic air showers will be briefly reviewed in the following section.[3]

3.1.2 Comparison of electromagnetic and hadronic air showers

If the incoming particle is a hadron, the nucleus scatters inelastically with the nuclei of the atmospheric molecules, interacts strongly and produces secondary particles like pions, kaons but also nucleons. In contrast to a purely electromagnetic air shower these hadron induced showers consist of two components, the hadronic component and many electromagnetic sub showers. Hadronic particles form the shower core and build up the electromagnetic component via decay products of neutral and charged mesons.

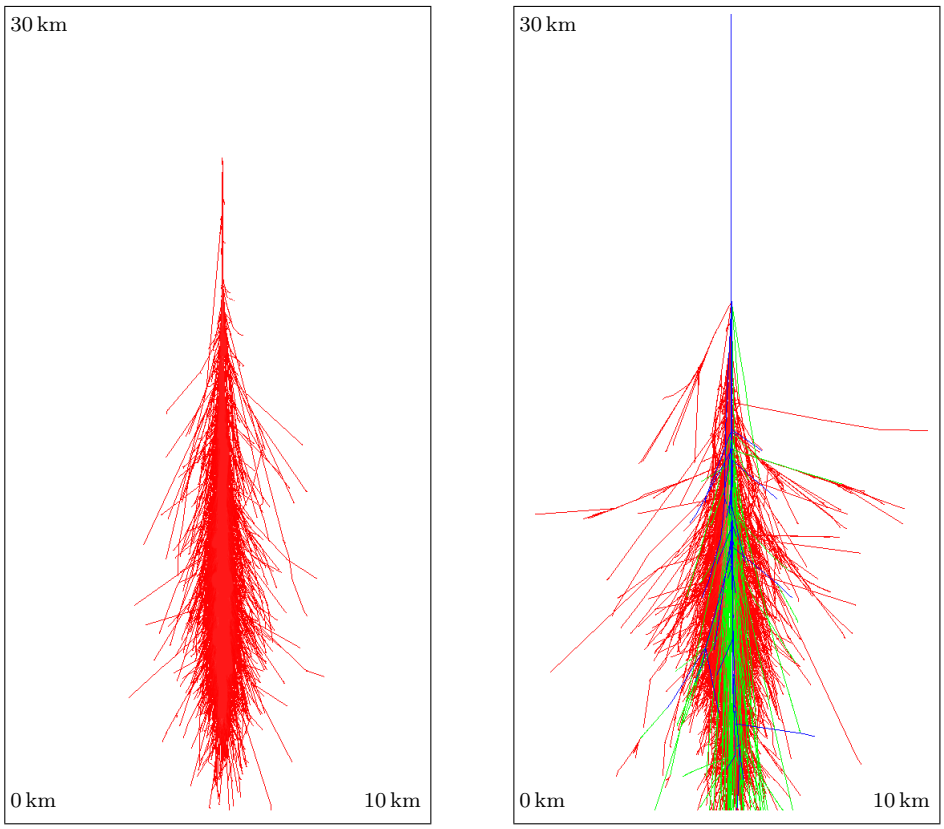

(a) γ-ray induced air shower with 300 GeV and first interaction in 23 km height

(b) hadron induced air shower with 1 TeV and first interaction in 18 km height

Figure 3.2: Simulations of γ-ray and hadron induced air showers (with courtesy of K. Valerius). A γ-ray initiated air shower consists only of an electromagnetic component (illustrated in red), whereas the hadron induced shower has apart from the hadronic component (blue) a distinct muon component (green) and electromagnetic sub showers (red).

Figure 3.2 compares a simulated electromagnetic and hadronic shower. Their different evolution allows a clear distinction. The mean free path for a proton with TeV energies is larger than the electromagnetic radiation length and due to this the depth of the shower maximum is larger

[3] For a more detailed discussion see for example refs. [25] and [26]

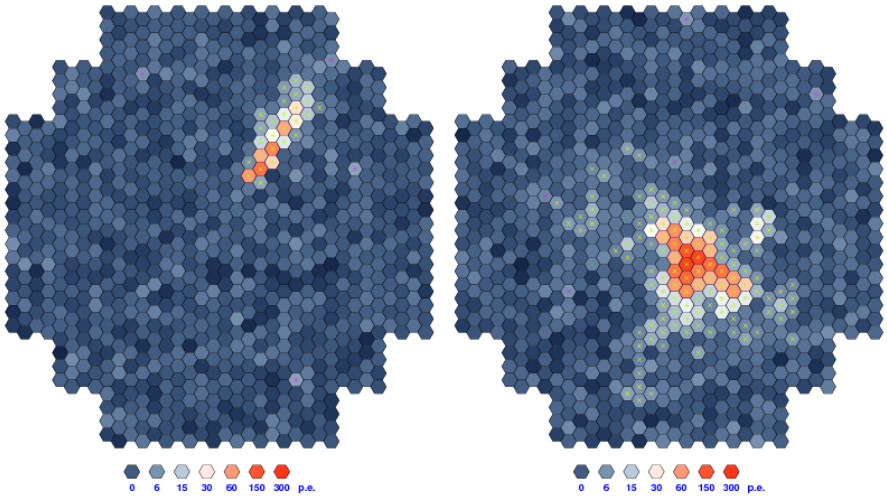

Figure 3.3: Camera images of a γ-ray induced air shower and a hadron initiated one (taken from [27]). The shape of the electromagnetic shower image shows an elliptical structure, whereas the image of the hadronic shower is more irregular.

than that of electromagnetic air showers at comparable energies. The lateral extension of an electromagnetic shower is smaller than for a hadronic one, because the lateral development of electromagnetic showers is dominated by multiple Coulomb scatterings and the mean scattering angle is smaller than for hadronic interaction and so the lateral extension is constrained. Hadronic showers involve more complex multi-particle processes and are less regular than electromagnetic showers because of the larger fluctuations. Figure 3.3 shows camera images of an 1 TeV γ-ray initiated air shower and of a 2.6 TeV proton initiated one. The electromagnetic shower image has an elliptical shape and can be parametrised as an ellipse (for definition of the Hillas parameters see Section 3.3), where as the image shape of an hadron induced air shower is more irregular because of the different shower evolution with more sub showers.

3.1.3 Differences between electron and γ-ray induced air showers

As discussed above hadronic and electromagnetic air showers evolve differently and this permits to separate them. However, cosmic-ray electrons and γ-rays both initiate electromagnetic air showers, which are very similar. Hence, it is difficult to distinguish electron induced from γ-ray initiated showers.

Yet, there is a feature, at least statistically, that gives a hint. Electrons interact in average immediately upon entering the atmosphere, whereas γ-rays interact deeper in the atmosphere. As a consequence the electron induced air showers reach their maximum at smaller depth than the γ-ray initiated showers. In approximation the depth of the electromagnetic air shower maximum can be estimated [28]:

$$X_{max}^{\gamma/e} = 1.01 X_0 \left(\ln \frac{E_0}{E_c} - n \right). \tag{3.3}$$

Here E_0 is the energy of the primary particle, E_c the critical energy where the shower development stops and X_0 is the radiation length in air. The quantity n is different for electrons ($n = 1$) and

γ-rays ($n = 0.5$) and leads to a constant offset in the depth of the shower maximum,

$$\Delta X_{max} = \Delta X^{\gamma}_{max} - \Delta X^{e}_{max} = \simeq 0.505\, X_0. \tag{3.4}$$

Note that this approach does not take into account the energy dependence of the shower maximum.

Sahakian et al. [29] analysed differences in shower evolution of electron and γ-ray initiated electromagnetic air showers in the energy range between 3 GeV and 100 GeV. In this energy region electrons can lead to an irreducible background for the observation of γ-rays from extended sources by low-energy threshold IACTs, which can not be cut down by traditional γ-ray/hadron separation methods. These authors consider energy-dependent altitudes of the shower maxima and use a simplified atmospheric model where the atmospheric density changes exponentially with height. ΔX_{max} can be written as:

$$\Delta X_{max}(E) = h_s \ln\left(1 + \frac{1}{2(\ln\frac{E}{E_c} - 1)}\right) \simeq \frac{h_s}{2(\ln\frac{E}{E_c} - 1)}, \tag{3.5}$$

where h_s is the scale height of the atmosphere (7.1 km) [29]. Hence, the difference in the depth of the shower maxima decreases with increasing energy of the primary electrons and photons. $\Delta X_{max}(10\,\mathrm{GeV}) \approx 1.14\,\mathrm{km}$ and falls to $\Delta X_{max}(100\,\mathrm{GeV}) \approx 0.57\,\mathrm{km}$. This offset further diminishes in the H.E.S.S. energy range, so a very sensitive reconstruction and analyses technique is necessary to use X_{max} as separation parameter. An advanced reconstruction technique provides also the depth of first interaction as an analysis parameter, so there are two parameters that are sensitive to the differences of electron and γ-ray initiated air showers. This motivated an attempt of electron/γ-ray separation (see Chapter 6).

The authors of [29] also considered effects of the deflection of charged secondary particles in the geomagnetic field which likewise affects the shower development. This increases the difference in shower evolution and affects the electron initiated showers more, because the primary particle is charged and the secondary charged particles are produced at higher altitudes and have more time to be efficiently deflected. This results in different lateral distributions and pulse forms of the Cherenkov light emitted by electron or γ-ray induced air showers in the energy range of the study below 100 GeV. Above this energy no study of a possible electron/γ-ray separation for imaging atmospheric Cherenkov telescopes is published.

3.2 Imaging atmospheric Cherenkov telescopes

The charged relativistic secondary particles of the induced air showers can emit Cherenkov light propagating through the atmosphere. The Cherenkov light produced by an air shower in the Earth's atmosphere can be observed either with a single IACT or an array of such telescopes as shown in figure 3.4(a).

If the velocity v of a charged particle in medium with refractive index n is larger than the speed of light in this medium c/n, the particle produces Cherenkov light due to the polarisation of the medium. This condition leads to an energy threshold E_{min} of

$$E_{min} = \frac{E_0}{\sqrt{1 - \frac{1}{n^2}}} \tag{3.6}$$

with the energy E_0 of the propagating particle. The charged particle polarises atoms along the trajectory trough a dielectric medium. Coherent light superimposed in wave fronts is emitted

during depolarising. These wave fronts form a light cone with an opening angle θ according to

$$\cos\theta = \frac{1}{\beta \cdot n}, \tag{3.7}$$

with $\beta = v/c$. The atmospheric refractive index n changes with variation in the density of the atmosphere. The opening angle for a 1 TeV γ-ray initiated air shower is approximately 1°.

This continuous spectrum of Cherenkov light extends over the optical and ultraviolet (UV) region. The relative intensity is approximately proportional to $1/\lambda^2$. There is a cut-off wavelength where v can not meet the condition $v > c/n$, because of the wavelength dependence of the refractive index $n(\lambda)$. Cherenkovh radiation emitted by air showers has its maximum intensity typically in the UV region.

γ-ray induced air showers have the shower maximum approximately between 8 and 10 km height and most of the UV Cherenkov photons are absorbed by ozone molecules before reaching the ground. But also intensities in optical wavelength are reduced, for example by Rayleigh scattering or Mie scattering off aerosol molecules in the atmosphere. About 100 Cherenkov photons per m^2 from one air shower emitted can be observed on the ground at 2000 m above sea level. Hence very large reflector areas are needed. IACTs observe the Cherenkov photons in the blue end of the optical region and the reflectors are optimised for these wavelengths.

As mentioned above the opening angle of the Cherenkov light cone for an 1 TeV γ-ray induced air shower is about 1°. Thus an air shower with a height of the shower maximum of about 8 km to 10 km illuminates an area on the ground with a radius about 130 m. The shower can be observed with every telescope within the illuminated area and this induces large effective detector areas compared with satellite-based astronomy.

The basic observation principle is illustrated in figure 3.4. An illuminated telescope collects the Cherenkov photons emitted by the air shower with its large collection area and projects the shower image onto the focal plane, where a sensitive camera is positioned and a shower image is taken.

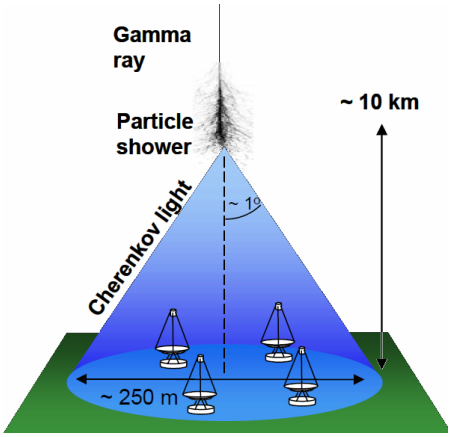

(a) A γ-ray interacts with the atmosphere and the initiated air shower emits Cherenkov light. All telescopes within the illuminated area can observe the shower.

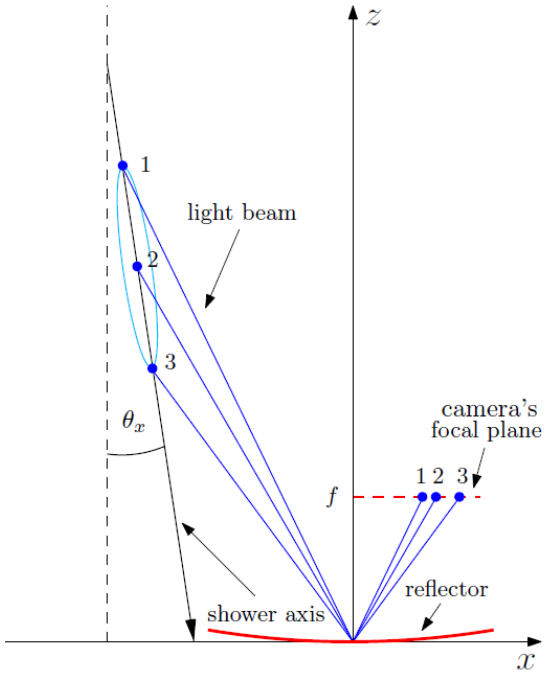

(b) Basic observation principle of an IACT. The Cherenkov photons emitted by the air shower are collected with large reflectors and projected onto the focal plane where a camera is positioned.

Figure 3.4: Observation of Cherenkov photons emitted by the air shower with telescopes.

3.3 The H.E.S.S. experiment

Figure 3.5: The four H.E.S.S. telescopes with the mirror dish for CT5 (in the middle) during the mirror exchange of CT3 (second from right) in April 2010

The name H.E.S.S. stands for High Energy Stereoscopic System and also honours Victor Hess, who discovered the cosmic rays with balloon experiments. The experiment is situated in the Khomas Highlands of Namibia at 1800 meters above sea level. This location was chosen for its good weather situation, many cloudless nights, almost no background light from nearby cities and unblocked view to the Galactic Centre. The H.E.S.S. telescope array, shown in figure 3.5, consists at the moment of four telescopes (CT1 throuh CT4) that are placed in a square formation with a side length of 120 m. The extension of H.E.S.S. with a fifth larger telescope (CT5) in the middle of the telescope array is under construction. CT5 is designed with larger mirror dish and reflector area. The telescope positions were optimised for a maximum sensitivity at the design energy threshold of 100 GeV for the four-telescope array. With the large reflector of CT5 the energy threshold decreases. The H.E.S.S. experiment has been taking data with four telescopes since 2003.

Mirror system

The telescope dishes are arranged in a hexagonal setup with a flat-to-flat diameter of 13 m. Each dish is composed of 382 round mirror facets with a diameter of 60 cm. The effective mirror surface is 107 m^2 per telescope. The mirror dish is mounted in an altitude-azimuth fashion on a rotating steel construction.

The mirror arrangement follows the Davies-Cotton layout [30], where all reflector facets have the same focal length f equal to the focal length of the telescope as a whole and the mirrors are mounted on a sphere with radius f. This mirror layout provides good imaging also for showers further away from the optical axis. The mirrors consist of aluminised optical glass with a protective quartz coating. Since the optical efficiency of the mirrors decreases with time, the mirrors of the telescopes need to be exchanged and refurbished in regular intervals. CT3 was the first telescope to receive new mirrors in April 2010. For a detailed description of the mirror system and alignment see [31] and [32].

Figure 3.6: The telescope CT3 during mirror exchange in April 2010. The round mirrors each with a diameter of 60 cm are mounted on a steel construction. The camera is positioned on a four arm system in the focal plane with 15 m distance to the reflector plane.

Camera

Each camera is mounted on a four arm system at the focal distance f of 15 m. The cameras consist of 960 photo-multiplier tubes (PMTs) arranged in a hexagonal array. The field of view (FOV) of a single PMTs relates to 0.16° in diameter on the sky, this yields for the whole camera a FOV of 5°. The single PMTs are enclosed by Winston Cones to capture the light that would fall between the tubes. It also limits the FOV of each tube in order to minimise the background light. The sample rate for one PMT is about 1 GHz.

The PMTs are grouped together in 60 drawers, each drawer consists of 16 PMTs. These drawers contain the trigger and readout electronics for the tubes, as well as the high voltage supply, control and monitoring electronics [10].

Trigger

H.E.S.S. makes use of a two-level trigger system - the first level on the camera and the second level is a central trigger that requires at least two telescopes triggering. A detailed description of the H.E.S.S. trigger and readout system is given in [33].

The camera trigger occurs if the sector threshold and the pixel threshold are exceeded. The sector threshold requires a signal in 3 PMTs in a sector of the camera, each camera being divided into overlapping sectors containing 64 pixels, and the pixel threshold requests more than 4 photoelectrons per pixel. The PMT signals are sampled with 1 GHz Analogous Ring Samplers with ring buffers. If a camera triggers, the ring buffer is stopped and the content is read out.

The central station receives information on all telescope triggers and if a valid coincidence of two or more telescopes occurs within 80 ns. The central trigger greatly reduces the read-out rate due

to avoiding night sky background and single muon events.

Calibration and reconstruction

H.E.S.S. observations usually are divided into single runs, each with 28 minutes of observation time. Each run has to pass different quality checks before being used for further analysis. This check tests, if there were any hardware problems or bad weather conditions that could affect the data quality. Runs that pass the quality control consist of $\approx 10^3$ triggered events. For each event two to four camera images are stored and from these images the energy and direction of the primary particle are reconstructed.

The first step is the calibration of these camera images. For each pixel the amplitude is converted from ADC values to photoelectrons (p.e.) and the pedestals (i.e. the null level of the PMTs) are subtracted. (For detailed description of the calibration see [34].)

The standard analysis [10] cleans the calibrated images before parametrising the shower image with so-called *Hillas parameters* [35]. During this cleaning only pixels are kept, that contain more than m p.e. and a neighbour more than n p.e. and vice versa. In the standard cleaning m and n have values of 5 p.e. and 10 p.e., but also cleanings with 5 p.e. and 7 p.e. are used. The shape of the cleaned shower image is approximately an ellipse and the *centre of gravity*, *image size*, *orientation* of the ellipse in the camera coordinate system, *length* and *width* are calculated. The image size is defined as the number of photo electrons contained in the cleaned image. *Length* is the length of the major axis of the ellipse and *width* refers to the length of the minor axis. Figure 3.7 illustrates the Hillas parameters.

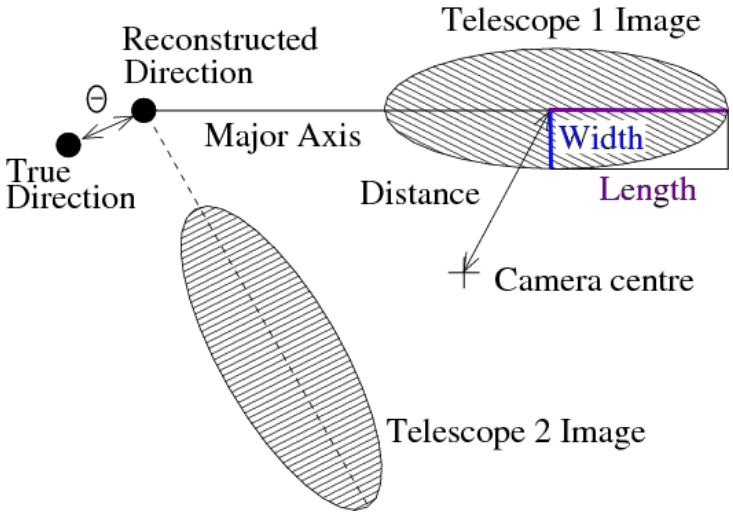

Figure 3.7: Schematic illustration of two shower images with the elliptic parametrisation (taken from [10]). The width and length are the minor respectively major axis. The direction is reconstructed by the intersection of the major axis.

H.E.S.S. is a stereoscopic telescope system and only events with more than two triggered telescopes are kept. The *shower direction* is reconstructed by the intersection of the major axis of superimposed shower ellipses in the camera system. If the event is observed with more than two telescopes the intersection is made pairwise and then weighted according to the uncertainties in the involved camera images.

The distance to the impact point where the extrapolated trajectory of the primary particle hits the ground, termed *impact distance*, is derived from intersection of the major axes in the coordinate system of the telescope array.

The Hillas parameters contain all information for the standard Hillas analysis [10] to reconstruct the shower direction, impact distance, the depth of shower maximum and energy of the primary particle. The depth of shower maximum is calculated from atmospheric profiles using the height determined from the angular distance of the centre of gravity to the reconstructed direction and impact distance. The energy of the primary particle is determined from the image size depending on zenith angle and impact distance from comparison with Monte Carlo simulations.

The model analysis [3] (see also section 4.1) uses these Hillas parameters as starting points for a fit comparing the real data camera images with model images (section 4.1). The energy of the primary particle, direction, impact and depth of first interaction are output parameters from this fit. This reconstruction technique is detailed described in Section 4.1.

The mirror reflectivity degrades over time and this leads to a decreased image intensity compared with Monte Carlo simulations. The optical efficiency can be monitored using single muon events close to the telescopes. The falling optical efficiency causes a shift in the absolute energy scale of the detector as the reconstructed energy of the events is too low. A correction factor for each telescope and run is applied to the reconstructed energy. For detailed information on energy correction see [36].

Chapter 4

Electron identification

This Chapter explains how electrons are identified, starting with the principles of an advanced air shower reconstruction technique in Section 4.1. The electron/hadron separation is performed with the Boosted Decision Tree (BDT) algorithm as described in Section 4.2 and the application to electron Monte Carlos and background data is described in Section 4.3. The remaining background is estimated by a χ^2 fit using models of the BDT response for electrons and protons from Monte Carlo simulations (see Section 4.4).

4.1 Reconstruction

For this analysis of high-energy cosmic-ray electrons a gamma-ray likelihood reconstruction technique (Model Analysis)[3] providing better sensitivity to electromagnetic air showers than the standard Hillas reconstruction techniques [10] was chosen. The Model Analysis also provides the depth of first interaction t_0 as an additional analysis output parameter that could give further information in view of a possible electron/γ-ray separation (see Chapter 6). This reconstruction technique is based on the comparison of the shower image taken by the camera with calculated shower images that are obtained from a model of the Cherenkov light distribution in electromagnetic air showers.

A semi-analytical shower model [3] describing the Cerenkov light distribution of charged particles in electromagnetic showers is used in the model reconstruction technique. This distribution is determined by the longitudinal, lateral and angular distributions of the particles in the shower which are derived from Monte Carlo simulations. Semi-analytical shower model means, that the distributions from the Monte Carlo simulations are parametrised to get an analytical description. Figure 4.1 shows examples of two-dimensional shower images.

Contrary to Hillas parameter based reconstruction techniques no image cleaning is necessary to extract the shower-related pixels, but the Hillas parameters derived from the cleaned image are used as starting parameters. The whole camera image can be used in the fit and the night sky background noise in the camera is also considered in the simulated camera images.

To obtain the most likely parameters of the incoming particle a minimisation procedure is used, that compares the intensity in each camera pixel with the predicted one from the model. Equation 4.1 [3] describes the probability density (likelihood) to observe a signal s in a pixel for an expectation value μ from the model prediction. It is given by a convolution of the photo-electron

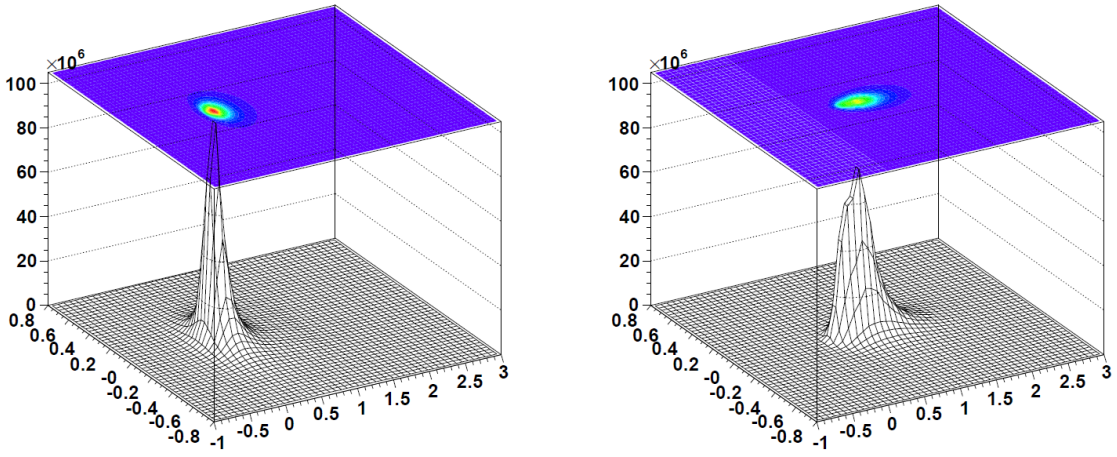

Figure 4.1: Model of a 1 TeV shower started at one radiation length and hitting the ground 20 m (left) and 100 m (right) and away from the telescope. X and Y axes are in units of degrees in the camera frame and the Z axis is the image amplitude (taken from [3]).

number n with the photomultiplier resolution. σ_p is the width of the pedestal and σ_γ the width of the single photo-electron peak that determines the photomultiplier resolution:

$$P(s|\mu,\sigma_p,\sigma_\gamma) = \sum_n \frac{\mu^n \exp(-\mu)}{n!\sqrt{2\pi(\sigma_p^2+n\sigma_\gamma^2)}} \exp\left(-\frac{(s-n)^2}{2(\sigma_p^2+n\sigma_\gamma^2)}\right). \tag{4.1}$$

For each pixel the log-likelihood is defined as:

$$\ln L = -2 \cdot \ln P(s|\mu,\sigma_p,\sigma_\gamma). \tag{4.2}$$

The Poisson distribution in equation 4.1 can be replaced at high μ by a Gaussian distribution with width $\sqrt{\mu}$ and the likelihood can be simplified to a convolution of two Gaussian distributions:

$$P(s|\mu \gg 0,\sigma_p,\sigma_\gamma) \approx \frac{1}{\sqrt{2\pi(\sigma_p^2+\mu(1+\sigma_\gamma^2))}} \exp\left(-\frac{(s-\mu)^2}{2(\sigma_p^2+\mu(1+\sigma_\gamma^2))}\right). \tag{4.3}$$

Starting from the pixel log-likelihood one can define a telescope log-likelihood as the sum over the log-likelihood of all pixels [3]:

$$\ln L_{tel} = \sum_i^{N_{pix}} \ln L_i = -2 \sum_i^{N_{pix}} \ln P(s_i|\mu,\sigma_p,\sigma_\gamma). \tag{4.4}$$

This telescope log-likelihood is used in the minimisation procedure to derive the best parameters for direction, impact parameter, depth of first interaction and energy of the primary particle. Good starting points are important for the fit procedure and are derived from estimates of the standard Hillas reconstruction technique.

The optical efficiency of each telescope is measured from ring-shaped images of muons passing through the telescope and is taken into account on reconstruction level, so there are no further energy corrections needed in the standard γ-ray analysis.

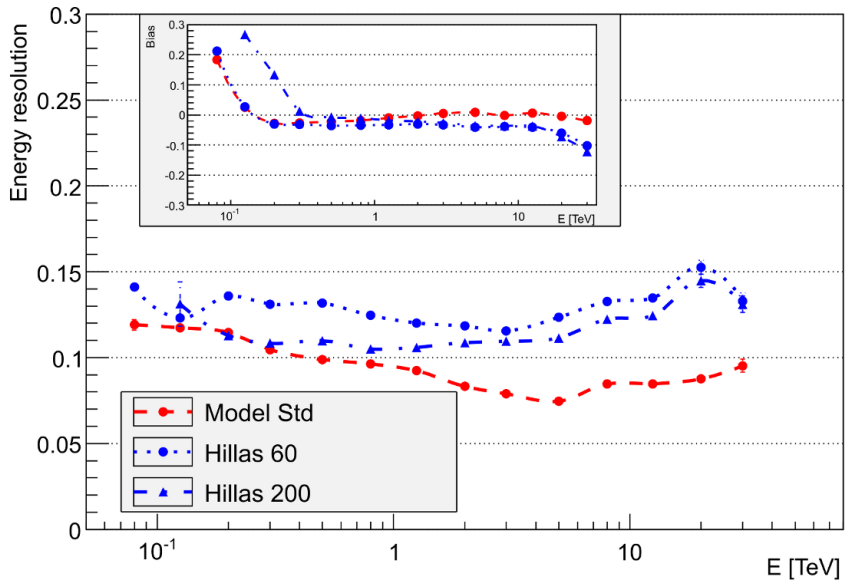

Figure 4.2: Energy resolution of the model reconstruction (red) compared with standard Hillas reconstruction (blue) (taken from [3]). Throughout the whole energy range the energy resolution of the model analysis is better than 15% and in a wide range better than 10%.

Figure 4.2 shows the energy resolution of the model analysis reconstruction (coloured in red) compared with standard Hillas reconstruction (see graphs in blue). In the whole energy range the energy resolution of the model analysis is better than 15% and in the core energy range between 500 GeV and 10 TeV below 10%. The energy resolution is defined as the root mean square of the $E_{reco} - E_{true}/E_{true}$ distribution. The energy bias is $\log(E_{reco}/E_{true})$.

For γ-ray analysis it is important to discriminate the γ-induced air showers from the hadron induced ones. For this purpose a variable called *Goodness of Fit*, G, is introduced and is defined as a normalised sum over all pixels of the difference between the actual pixel log-likelihood and its expectation value:

$$G = \frac{\sum_i^{N_{pix}} [\ln L(s_i|\mu) - \langle \ln L \rangle|_{\mu_i}]}{\sqrt{2 \cdot NdF}}. \tag{4.5}$$

NdF is the number of degrees of freedom. The Goodness of fit can be used to check the compatibility of the reconstructed shower with a pure γ-ray shower and hence for the discrimination between γ-ray and hadron-like events.

Similar to the Goodness of fit G a variable *Shower Goodness* (SG) is defined that takes into account only pixels belonging to the shower core.

For the γ/hadron separation several cuts are used and this separation is mainly based on the Shower Goodness and depth of first interaction. Table 4.1 summarises the cuts for standard analysis, the analysis of sources that are fainter than a few percent of the Crab flux and a configuration that maximises the γ-ray efficiency of strong sources, but with a diminished background rejection [3].

Table 4.1: Cuts for γ/hadron separation for standard analysis, analysis of faint sources and loose cuts for maximising the γ-ray efficiency of strong sources [3]. There are cuts applied to the minimal number of photo electrons (min. charge), the maximum distance from the camera centre (max. nom. dist.), the number of triggered telescopes (tels), the shower goodness (SG), the depth of first interaction (t_0) and the squared distance to the target position (θ^2_{max}).

name	min. charge [p.e]	max. nom. dist. [deg]	tels	SG_{max}	t_0 [X_0]	θ^2_{max} [deg^2]
standard	60	2	2	0.6	[-1,4]	0.01
faint Source	120	2	2	0.4	[-1,4]	0.005
loose Cuts	40	2	2	0.9	NA	0.0125

4.2 Electron/hadron separation with Boosted Decision Trees

In the last years multivariate classification methods, that are based on machine learning have been successfully used in VHE astronomy for γ/hadron separation (see [37] and [38]).

A multivariate classification method was used in this work because it very often provides a higher γ-ray efficiency than simple cuts and it also offers a possibility to estimate the remaining background for generating a electron spectrum. Usual background subtraction methods [39] can not be applied to the cosmic-ray electron analysis, because in this case due to the isotropically distribution on the sky no separation between on and off-data is possible.

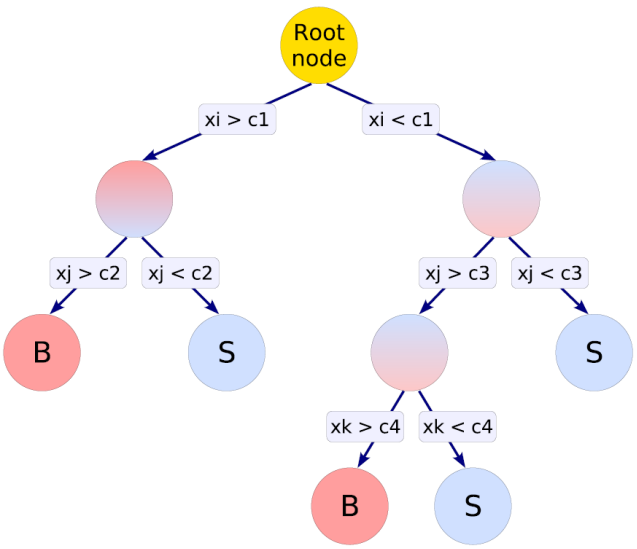

Figure 4.3: Schematic figure of one decision tree (taken from [40]). At each node there is a decision whether the value of the variable classifies the event as signal- (S) or background-like (B).

This work makes use of the Boosted Decision Tree (BDT) methods from the ROOT TMVA Toolkit [40] for the classification of signal- or background-like events. This method was chosen because it can take into account nonlinear correlations between input parameters and is not sensitive to parameters without separation power.

A schematic view of a decision tree using discriminating variables x_i is shown in figure 4.3. At

each node there is a binary decision whether the event is signal- or background-like. At the end one output parameter is obtained, that describes the signal- or background-likeness of one event.

Such decision trees, however, are unstable with respect to statistical fluctuations, so a forest of decision trees is constructed by a process called *boosting* in order to increase the stability of the algorithm. The most widely used boosting algorithm, which is also employed in this work, is the adaptive boost (AdaBoost). In this algorithm events, misclassified during the training phase, are given a weight α in the training of the next tree. This weight is determined from the fraction of misclassified events err as described in equation 4.6 and is renormalised after the application to all events of the training sample so that the sum of all weights remains constant:

$$\alpha = \frac{1 - err}{err}. \tag{4.6}$$

4.3 Application to electron/hadron separation

4.3.1 Monte Carlo simulations and data used for BDT training

Before using the Boosted Decision Tree algorithm for electron/hadron separation the BDT has to be trained with events that are known to be either signal or background.

For this training purpose diffuse electron Monte Carlo simulations were used as signal. The electron induced air showers were generated with KASKADE [41] and to these showers a specific detector simulation was applied to get generated shower images that are reconstructed similarly to shower images from real data (the employed reconstruction technique is described in Chapter 4.1).

The electron Monte Carlo simulations cover an energy range from 50 GeV to 100 TeV and the energy distribution follows a power law with an index of 2. This low power law index was chosen to get enough events for the training at higher energies. The BDT Output distributions are later weighted (see Section 4.4) to better match the expected spectrum. The simulations are generated at fixed zenith angles of 0°, 18°, 26° and 32° with an offset angle from the camera axis between 0° and 1.5°.

Data from observations targeting extragalactic fields with possible γ-ray sources excluded within a radius of 0.4° to the source position were used as background events. Extragalactic observations were chosen to avoid the diffuse galactic γ-ray background.

4.3.2 Energy and zenith angle bins

The BDT method uses different properties of the induced air showers to discriminate between signal- and background-like events. But most of the used parameters of air showers like depth of first interaction, depth of the shower maximum and also some of the Hillas parameters depend on energy and zenith angle, thus it is necessary to train in different energy and zenith angle bands.

The H.E.S.S. energy range from 100 GeV to 100 TeV was divided into six energy bins (same energy bins as in [37] and [38]) and the zenith angle range for this electron analysis from 0° to 30° was divided into three bins. Those were adjusted to the fixed zenith angles of the electron Monte Carlo simulations. The energy and zenith angle bins are summarised in table 4.2.

Table 4.2: Energy and zenith angle bins for Boosted Decision Tree training

Energy [TeV]	0.1-0.3	0.3-0.5	0.5-1.0	1.0-2.0	2.0-5.0	5.0-100.0
Zenith angle data	$0° - 14°$		$14° - 22°$		$22° - 30°$	
Zenith angle MC	$0°$		$18°$		$26°$	

4.3.3 Training parameters and BDT settings

For a good electron/hadron separation it is necessary to train the BDT with shower variables that show a good discrimination power. For the H.E.S.S. measurement of the energy spectrum of high-energy electrons [1, 4] primarily the Hillas parameters were input variables for the BDT training. Additionally the depth of shower maximum and energy resolution were chosen.

In this work instead of the standard Hillas reconstruction the reconstruction technique described in Section 4.1 was used. One motivation for using this model reconstruction is that it provides the depth of first interaction as additional reconstruction output parameter. The following variables were chosen as BDT input parameters:

- the depth of first interaction (t_0),
- the Mean Scaled Shower Goodness (MSSG),
- and Mean Scaled Background Goodness (MSBG)

from the model analysis, as well as

- the depth of the shower maximum (t_{max}),
- the Mean Scaled Width (MSW),
- the Mean Scaled Length (MSL)

from the Hillas reconstruction.

Figure 4.4 shows the distributions of the selected variables for the energy range between 0.5 TeV and 1.0 TeV and for zenith angles between 14° and 22°.

The depth of first interaction

The *depth of first interaction* t_0 of the primary particle with the atmosphere is a direct output parameter of the model reconstruction (see Chapter 4.1). Electrons interact very soon after they enter the Earth's atmosphere, mostly between 0 and 1 radiation lengths X_0, whereas the distribution of the first interaction point of hadrons is much broader. The spike at 5 X_0 in the background events is a reconstruction artefact [3]. Shower models are only generated for depths of 0, 1, 2, 3, 4 and 5 X_0. Between this values there will be interpolated and extrapolated above 5 X_0.

Mean Scaled Shower Goodness and Mean Scaled Background Goodness

The shower goodness was already mentioned in Chapter 4.1. It describes the goodness of fit only for pixels belonging to the shower. The *Mean Scaled Shower Goodness* (MSSG) is calculated from the individual telescope Shower Goodness. The average value $\langle SG_{tel}(q, \rho)\rangle$ and variance of

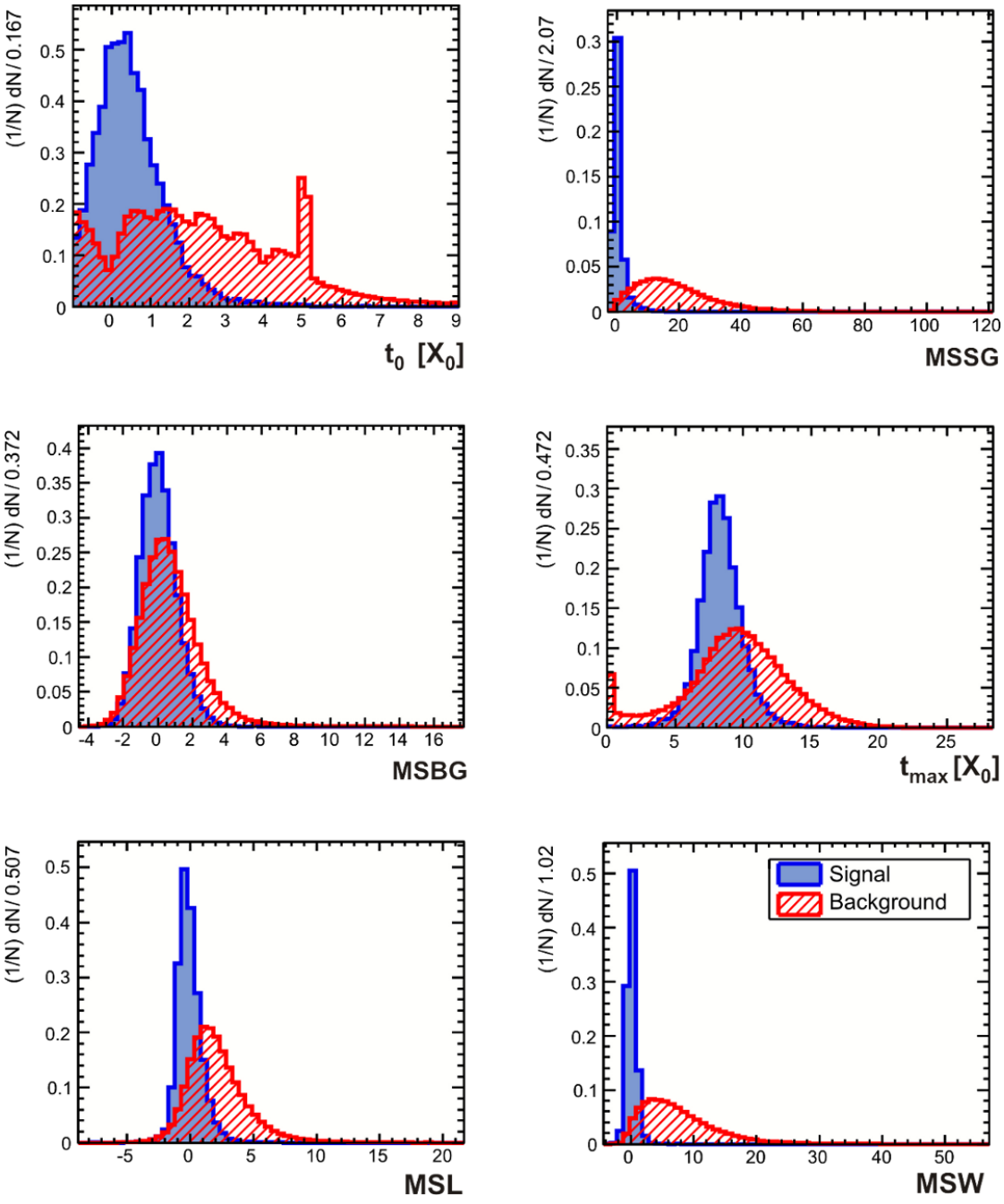

Figure 4.4: Distribution of input parameters for the Boosted Decision Tree Training for energies between 0.5 TeV and 1.0 TeV and zenith angles between 14° and 22°. In blue the distributions of the electrons as signal and in red the off-data events as background are shown.

the telescope Shower Goodness $\sigma_{tel}(q,\rho)$ as a function of image size q and impact distance ρ are compared to the actual Shower Goodness $SG(q,\rho)$ [42]:

$$MSSG = \frac{1}{\sqrt{N_{tel}}} \sum_{tel=1}^{N_{tel}} \frac{SG_{tel}(q,\rho) - \langle SG_{tel}(q,\rho)\rangle}{\sigma_{tel}(q,\rho)}. \tag{4.7}$$

The *Mean Scaled Background Goodness* (MSBG) is defined analogously to the Mean Scaled Shower Goodness.

The depth of shower maximum

Due to the different interaction cross sections for electrons and hadrons the distribution of the depth of first interaction between electron and hadron induced air showers differs and likewise the distributions of the *depth of the shower maximum* t_{max} differ for electrons and hadrons. Again the distribution for hadrons is broader than the one for electrons and the position of the maximum is also at lower values for electrons. The peak at 0 X_0 in the background distribution is again a reconstruction artefact with no physical meaning.

Mean Scaled Width and Mean Scaled Length

The width w and length l of the actual shower image are taken, as is the depth of shower maximum, from the Hillas reconstruction. Similar to the definition of Mean Scaled Shower Goodness the width and length are compared with expectation values and variance obtained from simulation as a function of the image charge q and impact distance ρ. The *Mean Scaled Width* (MSW) and *Mean Scaled Length* (MSL) are defined as [42]:

$$MSW = \frac{1}{\sqrt{N_{tel}}} \sum_{tel=1}^{N_{tel}} \frac{w_{tel}(q,\rho) - \langle w_{tel}(q,\rho)\rangle}{\sigma_{w,tel}(q,\rho)}, \tag{4.8}$$

$$MSL = \frac{1}{\sqrt{N_{tel}}} \sum_{tels=1}^{N_{tel}} \frac{l_{tel}(q,\rho) - \langle l_{tel}(q,\rho)\rangle}{\sigma_{l,tel}(q,\rho)}. \tag{4.9}$$

BDT settings

As mentioned in Chapter 4.2 the BDT method provided by the TMVA package was used for training and classification. The advantage of the BDT method is that it allows to consider also non-linear correlations between the input parameters, but the drawback of this method is a possible overtraining that can lead to bias effects. Thus it is very important to control the classification with an independent test sample and carefully study the different BDT settings. The number of trees for the forest was set to 200. The adaptive boost method (*AdaBoost*) was chosen for boosting. The training of a decision tree is determined by the definition of the splitting criterion for each node. It starts at the root where an initial splitting criterion is chosen and the splitting into subsets is continued until the number of events in a node falls below $N_{min} = \max(20, N_{train}/(N_{var}^2 \cdot 10))$ with the number of training events N_{train} and number of training variables N_{var}. The *Gini Index*[1] was chosen as splitting criterion. The splitting criterion is a cut on a single variable and the training determines the variable and the cut value that increases the separation index between the actual node and the sum over the indices of the

[1]The Gini Index is defined as $p(1-p)$[40], where p is the "purity" of the signal sample that is derived with a cut on the variable in this node. The purity can be described as $p = N_S/(N_S+N_B)$ with N_S the number of signal events and N_B the number of background events remaining in the sample. The Gini index has its maximum at a purity of 0.5.

two daughter nodes. The best cut value is derived by a scan over the variable with 200 steps. After growing the tree a process called *pruning* is applied which removes statistically insignificant nodes and reduces a possible overtraining of the tree. The pruning algorithm *Cost Complexity* was chosen. This algorithm compares the fraction of misclassified events of this node with and without further splitting in the sub tree. The prune strength was set to 20.

4.3.4 Correlation matrices and the importance of the training parameters

As already mentioned above it is important to choose suitable parameters for a successful signal/background separation. There are some possibilities to determine whether the parameter selection is useful or not. The TMVA-Toolkit gives an overview about the correlations between the used parameters in correlation matrices for signal and background. Figure 4.5 shows an example for the training bin with energies between 0.5 TeV and 1 TeV and zenith angles between 14° and 22°.

Most of the used input parameters show no or only weak correlations to other parameters. This is favourable for the separation because the separation power of the method can be enhanced by adding more parameters. If only strongly correlated parameters are used then there is no additional gain in using more parameters during the training and classification.

The example given in figure 4.5 also shows a few stronger correlations between some input parameters. For the signal events the depth of first interaction (t_0) and Mean Scaled Length (MSL) and also depth of first interaction and depth of shower maximum (t_{max}) exhibit a relatively high degree of correlation. These correlations are not surprising because both the depth of shower maximum and the Mean Scaled Length depend on shower evolution and hence on the depth of first interaction. The later the first interaction of the primary particle takes place the later the shower can reach its maximum extension. The width of the shower ellipse also depends on the point of first interaction, but not as strong as like the distribution of the length. Although, there is a strong correlation between the shower maximum and the depth of first interaction, both parameters were kept for testing, if these parameters provide additional information for a possible electron/γ-ray separation (see Chapter 6).

The background correlation matrix shows the largest coefficients between the Mean Scaled Length (MSL) and the Mean Scaled Shower Goodness (MSSG) and similarly with the Mean Scaled Background Goodness (MSBG). There is also a strong correlation between the depth of first interaction and the depth of shower maximum.

In conclusion there are different correlations between the input parameters for signal and background except the correlation between the depth of shower maximum and depth of first interaction, which is strong in both cases. These different correlations of the signal and background input parameters also show a choice of sensitive training parameters.

A possibility to rank the separation power of the various used training parameters is their importance during the training. This importance is composed of the rate of occurrence of a splitting variable during the training, weighted by a squared separation-gain and the number of events in the corresponding node ([37] and references therein). The importance of the different input parameters for zenith angles between 26° and 30° is shown in figure 4.6, which also illustrates the energy dependence of the importance. Notably the importance ranking changes at almost each transition between adjacent energy bins and all input parameters have an importance $> 10\%$ in at one energy bin. This also shows, the parameter choice is suitable.

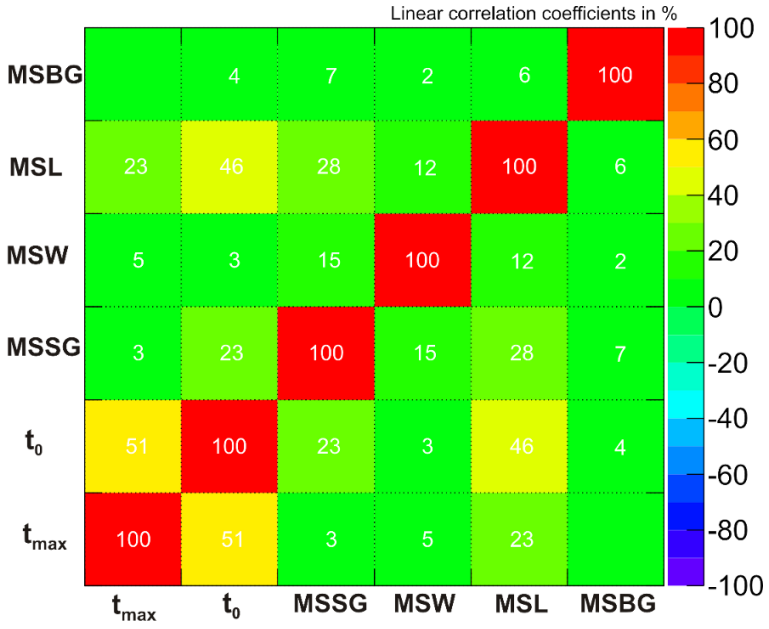

(a) Correlation matrix signal

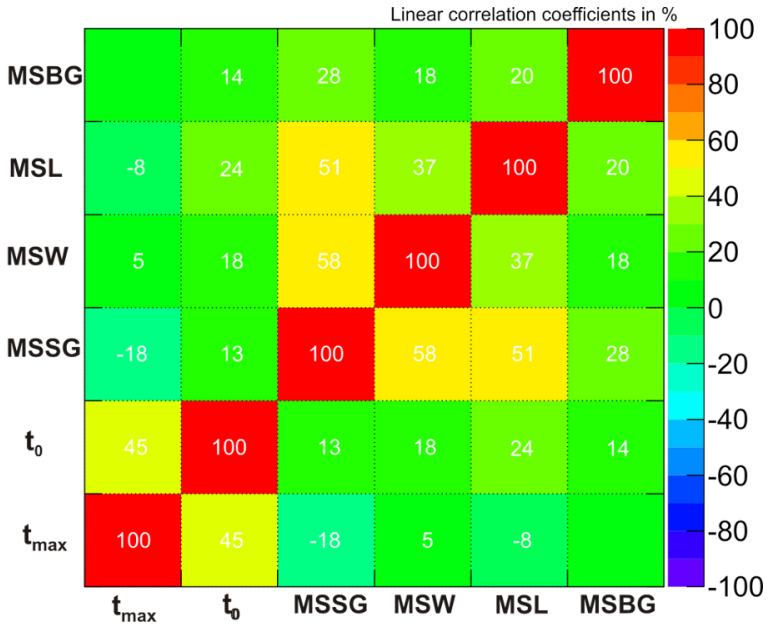

(b) Correlation matrix background

Figure 4.5: Correlation matrices for signal and background for energies between 0.5 TeV and 1 TeV and zenith angles between 14° and 22°. There are different correlations between the input parameters for signal and background.

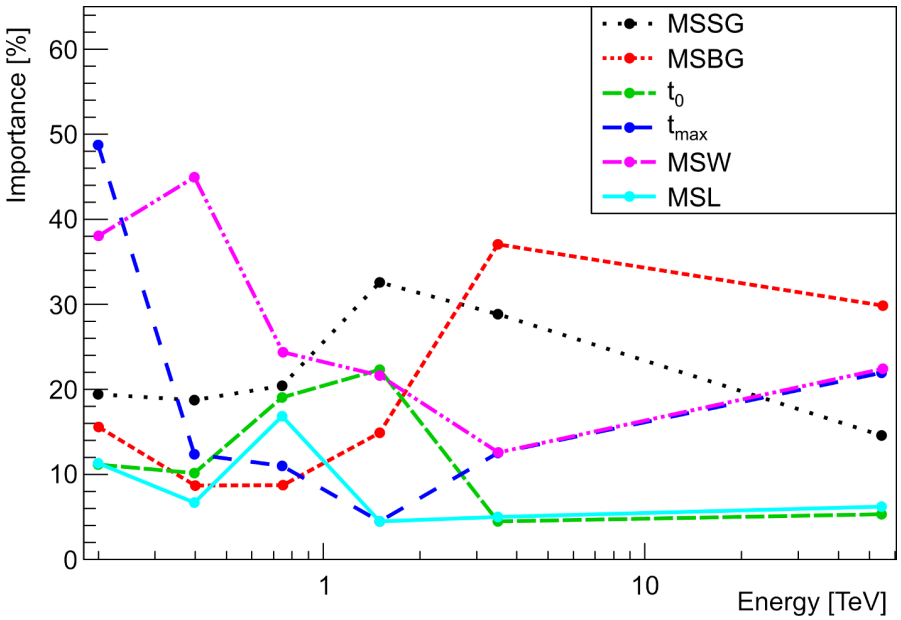

Figure 4.6: Importance of the training parameters as a function of energy at zenith angles between 26° and 30°.

4.3.5 BDT response and electron/hadron separation

The BDT method takes the above mentioned input parameters and determines for each event one output parameter, the BDT response, that describes the signal- or background-likeness of the event. The training of the Boosted Decision Trees was applied to an independent test sample and an example for the output distribution of signal and background events for energies between 0.5 TeV and 1 TeV and zenith angles between 14° and 22° is shown in figure 4.7. In this figure the BDT output distributions of the training and test sample are superimposed which allows to check the BDT classification for overtraining. If some overtraining occurs, the BDT response of training and test sample are expected to differ strongly. Here both the training and test distributions match very well, so there is no overtraining. The BDT output distributions for all training bins of energy and zenith angle are shown in Appendix A.

The electron/hadron separation is carried out by one cut on the BDT output parameter instead of cuts to each parameter. As shown in figure 4.7 above a clear electron/hadron separation is possible. For the electron analysis a cut value of the BDT output of 0.0 was chosen. This value was determined by evaluating the BDT response at which a maximum quality factor[2] occurs for the different energy and zenith angle bins (see figure 4.8(a)).

4.3.6 Performance

As already shown with the BDT output distributions of the signal and background events, this BDT analysis can clearly separate between signal and background on an event-by-event basis. One possibility to compare the performance of different cuts is the quality factor Q, which is

[2]The quality factor Q is defined as ratio of the signal efficiency and square root of the background efficiency, see equation 4.10.

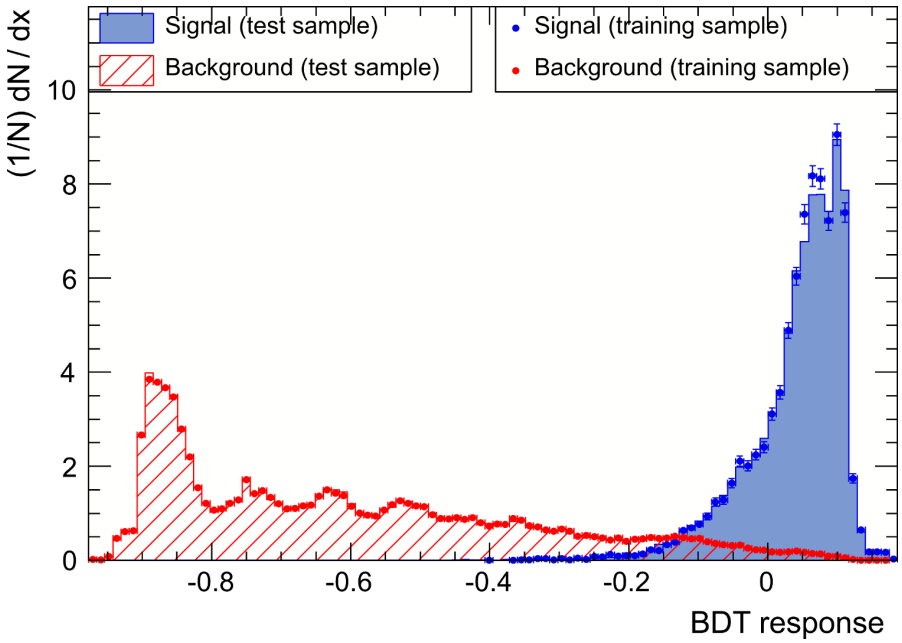

Figure 4.7: Distributions of the Boosted Decision Tree response for an independent test sample for energies between 0.5 TeV and 1.0 TeV and zenith angles between 14° and 22°.

defined as the ratio of the signal efficiency[3] ϵ_{sig} and the square root of the remaining background efficiency ϵ_{bg}:

$$Q = \frac{\epsilon_{sig}}{\sqrt{\epsilon_{bg}}}. \tag{4.10}$$

To get an estimate of the performance of this analysis the signal efficiencies for the maximum quality factor are presented in figure 4.9(a). The signal efficiency ranges from 43% to 69%. In all energy and zenith angle bins the remaining background is between 0.1% and 1.8%. This leads to high quality factors (values between 4.2 for energies $0.1 - 0.3$ TeV and zenith angles between 14° and 22° and 9.02 for the energy range between 2.0 TeV and 5.0 TeV and zenith angles below 14°). The corresponding distribution is shown in figure 4.8(b).

Figure 4.9(b) compares the quality factor Q_{BDT} of this BDT analysis with that of the model analysis Q_{MSSG} with the standard cuts that are summarised in table 4.1 (Chapter 4.1). Those standard cuts are mainly based on the shower parameter Mean Scaled Shower Goodness and the charge, but there are also additional cuts regarding the depth of first interaction and the distance to the camera centre.

It stands out that the BDT cut provides a better quality at the low energies ($0.1 - 0.3$ TeV) and at very high energies ($5.0 - 100.0$ TeV) than the model analysis standard method. In the energy training bins between 0.3 TeV and 0.5 TeV and between 2.0 TeV and 5.0 TeV both quality factors are comparable, but only in the energies between 0.5 TeV and 1.0 TeV and between 1.0 TeV and 2.0 TeV the BDT cut is worse than the model standard cut. But this does not surprise because the model standard cuts were optimised at these energies and for the BDT analysis used in this work almost no emphasis was placed on optimisation. This also shows that multivariate classification methods could give comparable or in some bins also better quality results than simple cuts even without any particular optimisation work.

[3]The efficiency is defined as the fraction of events from the signal or background sample which pass the BDT cut.

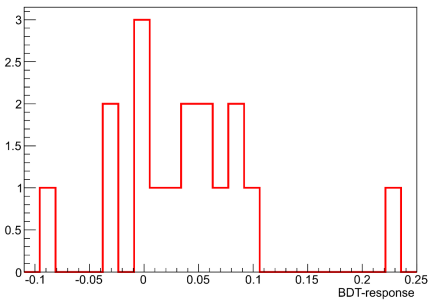

(a) Distribution of BDT response, where a cut on it maximises the quality factor for each energy and zenith angle bin.

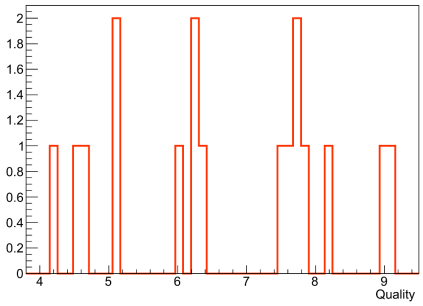

(b) Distribution of the maximum quality factor for each energy and zenith angle bin.

Figure 4.8: Figure 4.8(a) shows the distribution of BDT response with maximum quality factor for each energy an zenith angle bin. The average is at a value of 0.03 BDT response. The distribution of the maximum quality factor is presented in figure 4.8(b), where the BDT analysis has an average quality factor of 6.6.

4.4 Background determination

In the previous sections of this Chapter the reconstruction of events and the electron/hadron separation are described, but with just the cut on the BDT response not all remaining background can be rejected. Thus it is necessary to estimate the remaining background after the BDT cut. In analyses of γ-ray sources usually sky regions without known γ-ray sources are taken as off-regions and the background is subtracted (for a detailed description of ring background and on-off background models see [39]). It is not possible to apply the same strategy to a cosmic-ray electron analysis, since electrons are isotropically distributed and due to this no electron-free region of the sky can be used for background subtraction.

Instead, the background estimation is carried out with the help of Monte Carlo simulations. The BDT classification is applied to electron and proton simulations. The BDT output distributions are energy dependent and because of this, a correction due to the spectral shape has to be applied. This is a correction to the spectral index of the simulated proton and electron events, because they are simulated with a spectral index of 2 in contrast to the expected index to get also enough statistics at high energies. Each BDT response distribution is weighted with $(E/E_{min})^{-(\Gamma_{sim}-\Gamma_{exp})}$. E is the reconstructed energy with the optical efficiency correction applied already on reconstruction level, E_{min} should be a value below the energy threshold, which ensures that the weighting factor is smaller than one. Γ_{sim} denotes the spectral index of the simulations and Γ_{exp} an expected value. For protons Γ_{exp} would be 2.7 and for electrons about 3.3 or lager. This weighting procedure is described in [14].

The remaining background is now estimated by a fit using the weighted proton and electron distributions to match the BDT distribution of the remaining events. This fit is applied in the energy and zenith angle bins from the BDT training. A simple possibility to fit the distribution is to use a χ^2-minimisation. The value χ^2 is defined as

$$\chi^2 = \sum_i^{N_{bin}} \frac{(d_i - m_i)^2}{\sigma_{d_i}^2 + \sigma_{m_i}^2}. \tag{4.11}$$

The number of events in bin i of the data is given by d_i, the number of events in this bin of the model distribution consisting of protons and electrons is denoted by m_i, σ_{d_i} and σ_{m_i} are

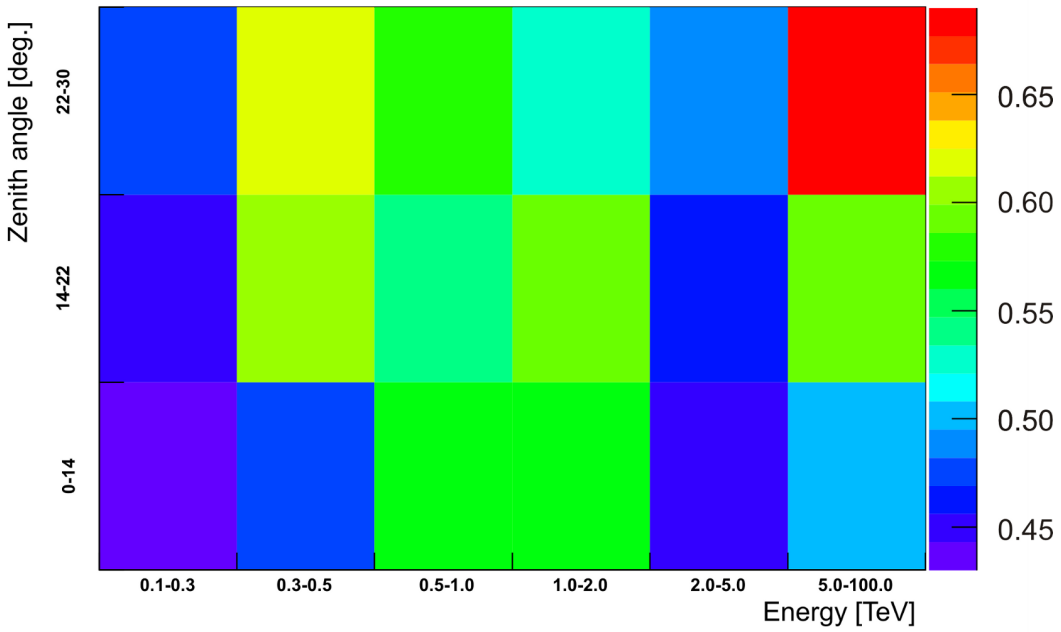

(a) Signal efficiencies for the BDT analysis at maximum quality factor

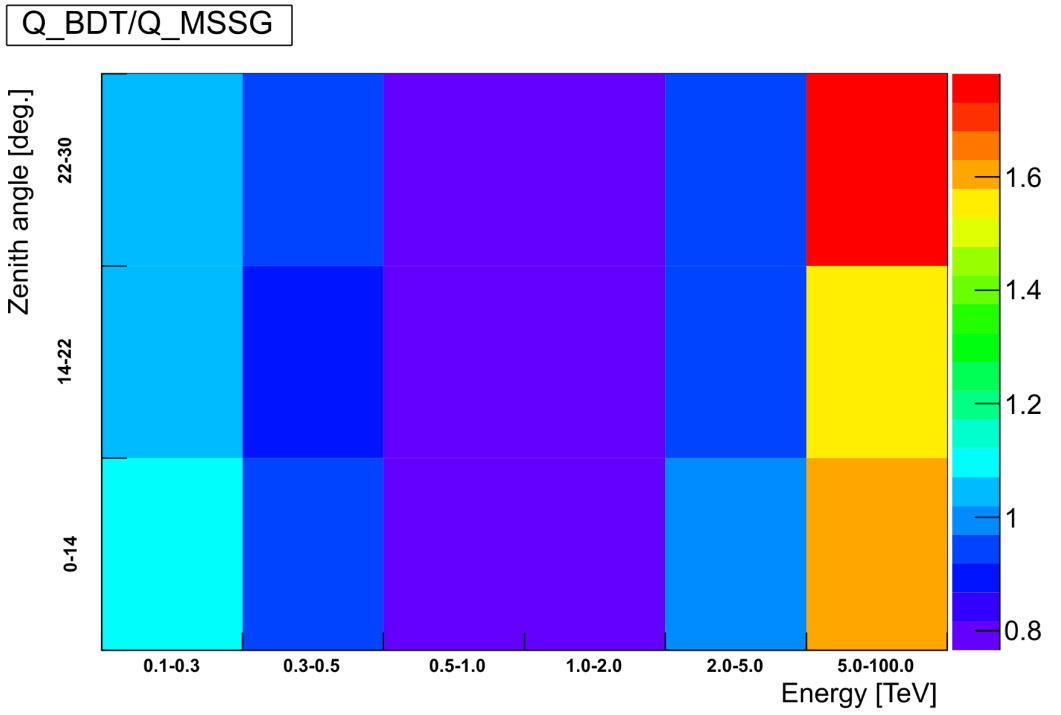

(b) Comparison of the quality factor of this BDT analysis with that of the model analysis with standard cuts

Figure 4.9: Signal efficiencies at the maximum quality factor of the BDT analysis and comparison of the quality factor with that of the model analysis with standard cuts.

the corresponding standard deviations. m_i consists of $n_{e,i}$ electrons and $n_{p,i}$ protons from the bin i of the simulated BDT response distributions. These distributions are normalised and the multiplying factor is varied step by step. The minimum of χ^2 yields the most likely composition of the data.

A more sophisticated approach contains a likelihood fit to estimate the remaining background (see [14]).

Chapter 5

Spectrum determination

The previous Chapters gave an introduction to high-energy cosmic-ray electrons, presented the H.E.S.S. experiment and described the necessary steps to separate electrons from background events. One important component to get the energy spectrum of a source is the effective collection area. Thus this Chapter gives an overview of the differential energy spectrum in Section 5.1, data selection in Section5.2 and effective collection area (Section 5.3) with emphasis on the different dependencies of the collection area and energy threshold.

5.1 Differential energy spectrum

The differential energy spectrum is defined as the number of electrons $N(E)$ per energy bin ΔE and solid angle Ω, livetime of the observation T and effective collection area $A_{\text{eff}}(E)$:

$$\frac{dF}{dE} = \frac{N(E)}{A_{\text{eff}} \cdot \Delta E \cdot T \cdot \Omega} \tag{5.1}$$

The number of electrons $N(E)$ is obtained through a separate BDT analysis for each energy bin ΔE. The remaining hadronic background is subtracted using models of the electron and hadron BDT response distributions as described in Sections 4.3.5 and 4.4.

The effective collection area A_{eff} is derived from Monte Carlo simulations and depends on energy, zenith angle, offset from the camera centre, optical efficiency and used cuts of the event selection. For a more detailed discussion of the effective collection area see Section 5.3.

5.2 Data selection

The data selection implies constraints both on the run selection and on the event selection. The run selection assures a good quality of the observations and does not influence the effective area directly. The event selection is a preselection before the electron/hadron separation of the BDT response cut, which directly influence the effective area. The effects of the run selection are indirect, for example via the optical efficiency of the chosen run or via the range of zenith angles (see Section 5.3).

For a run to pass the selection the following criteria have to be fulfilled:

- The mean zenith angle is between 0° and 30°. This constraint is due to the proton Monte Carlo simulations used in the H.E.S.S. measurement [1, 4], that were only produced for a zenith angle of 20°.
- The observation target is extragalactic to avoid the diffuse galactic γ-ray emission as additional γ-ray background.
- Variations in the trigger rate are less than 10% during the run to exclude cloudy observations. The trigger rate is larger than 1.2 times the expected trigger rate to exclude runs with dusty, hazy atmosphere, that can not be spotted in fluctuations in the trigger rate.
- Observations with all four telescopes working without technical problems to match the later event criterion of four triggered telescopes see below.

Each event of the selected runs has to pass the following criterions:

- The number of photoelectrons in the shower image is larger than 60, respectively 120, this is also called charge cut.
- All four telescopes triggered.
- The centre of gravity of the shower ellipse is within a distance of 2° from the camera centre,
- Any known or potential γ-ray sources are excluded within 0.4° from the source position.

These selection cuts only lead to a good event selection, not to a hadron/electron separation, but they also effect the effective collection area. The electron/hadron separation is carried out with a cut on the BDT response, which also effects the effective areas.

5.3 Effective collection area

The effective collection area is determined with Monte Carlo simulations and is defined as the ratio of the number of selected events N_{sel} and simulated events N_{MC} multiplied with the simulated effective area A_{MC}:

$$A_{\text{eff}}(E, z, \theta, \phi, o) = \frac{N_{sel}(E, z, \theta, \phi, o)}{N_{MC}(E, z, \theta, \phi, o)} \cdot A_{MC}(E, z, \theta, \phi, o). \tag{5.2}$$

It is a function of the true energy E, the zenith angle z, the offset from the camera centre θ, the azimuth angle of the telescope ϕ and the optical efficiency o. N_{sel} is the number of events that passes the trigger, data selection (see Section 5.2) and cut to the BDT response.

A set of tables with effective areas is calculated for fixed energy values, zenith angles 0°, 18° and 26°, offset from the camera axis between 0° and 2° with steps of 0.5°, azimuth angle 0° and 180°, optical efficiencies 50%, 60%, 70%, 80%, 90% and 100%. Between these fixed values the effective areas are interpolated.

Figure 5.1 summarises different dependencies of the effective areas. The step-like features in the effective areas are a result of the bin-wise application of the BDT classification.

The influence of the offset from the camera axis is shown for a zenith angle of 26° and optical efficiency 70% in figures 5.1(a) and 5.1(b). The effective collection area decreases with increasing distance to the camera axis. Also a different charge cut of 60 p.e. and 120 p.e. effects the effective

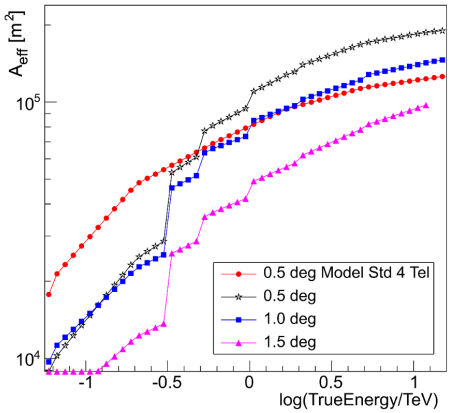

(a) Comparison of the effective areas at different offsets from the camera centre at a zenith angle of 26° and optical efficiency of 70% with a charge cut of 60 p.e. The effective area for model standard cuts (see Chapter 4.1) with only 4 telescopes events for an offset of 0° and zenith angle of 26° is applied in red.

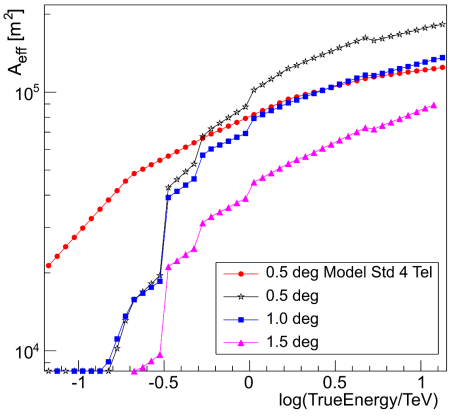

(b) Comparison of the effective areas at different offsets from the camera centre at a zenith angle of 26° and optical efficiency of 70% with a charge cut of 120 p.e. The effective area for model standard cuts are as well applied.

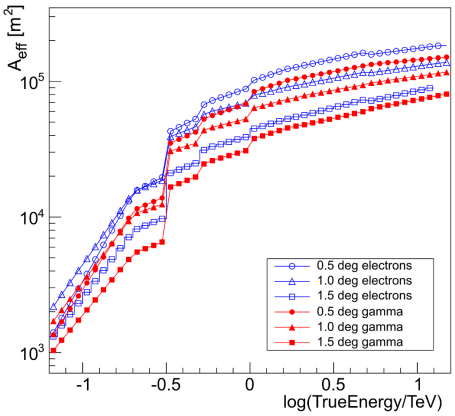

(c) Effective areas from 5.1(b) derived from electron simulations are compared with effective areas with the same cuts derived from γ-ray simulations. The effective areas from γ-ray simulations are systematically smaller.

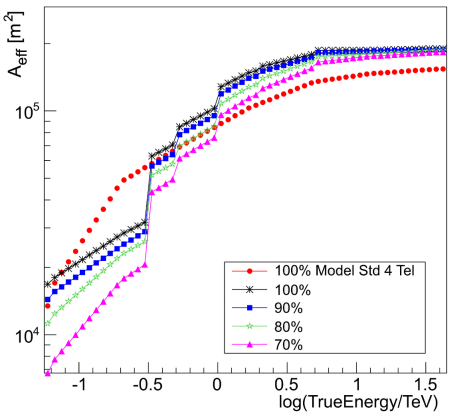

(d) Effective areas for optical efficiencies between 100% and 70% at the camera centre and zenith angle of 26°. The effective area for model standard cuts with 4-telescope events at the same zenith angle and camera centre is again included in red. These effective areas are derived from γ-ray simulations.

Figure 5.1: The effective collection area depends on energy, zenith angle, offset from the camera axis and optical efficiency. Figure 5.1(a) and 5.1(b) show the dependency on offset to the camera axis for charge cuts of 60 and 120 p.e., respectively. A lager charge cut results in smaller effective areas at low energies. For better comparison the effective areas derived for model standard cuts with 4 telescope events are applied.
In figure 5.1(c) the effective areas derived from electron and γ-ray simulations are compared and this shows that γ-ray effective areas are systematically smaller than the ones derived from electron simulations.
deteriorated optical efficiency of the telescopes results in decreasing effective areas, as shown in figure 5.1(d).

area, resulting in smaller effective areas at low energies with a higher charge cut. In both figures the effective area for γ-rays with model standard cuts and restriction to only 4-telescope events is included as a reference. Above 300 GeV the effective areas for data selection and BDT response cut (BDT response > 0.0) are of the same order or larger than the one for the model standard cuts. Below 300 GeV the effective areas are smaller due to the fact that the BDT cut is fixed to a single value for all energies, while the maximum quality factor for energies between 100 GeV and 300 GeV is achieved at a BDT response below 0.0, which was chosen as cut value. That leads to the reduced effective areas at low energies and can be avoided by introducing a low energy BDT response cut.

Both electrons and γ-rays initiate electromagnetic air showers, but there are differences in the shower evolution, which also effect the effective collection areas. Figure 5.1(c) compares the effective collection areas at a zenith angle of 26° and an optical efficiency of 70% for three different offsets from the camera centre. In all three offsets the effective collection areas derived from γ-ray simulations are smaller than the ones for electrons. This would result in systematically higher fluxes for electrons if the flux would be derived using collection areas determined from γ-rays. Thus it is necessary for electron spectrum determination to use effective areas for electrons and they can not be replaced by effective areas for γ-rays.

In figure 5.1(d) the influence of the optical efficiency on the effective collection area is illustrated. Reduced optical efficiency leads to decreased effective areas because the intensity of the shower image is reduced and less events pass the charge cuts. This leads to an increased energy threshold. These effective areas are derived from γ-ray simulations, because electron simulations were not available for all optical efficiencies, but this trend is the same for effective areas for electrons.

Taking the optical efficiencies and source extension into account

The effective collection area, needed to calculate the differential energy spectrum as defined in equation 5.1, is a mean effective collection area in different ways. Two aspects have to be taken into account. First, almost each run has a different optical efficiency and, second, the effective area has to be calculated in the same way as for extended sources, because of the dependency of the distance to the camera axis as shown in figure 5.1(a) and 5.1(b).

To handle the different optical efficiencies, for each run an averaged collection area A_{eff}^{run} is determined. The resulting effective collection area for the energy bin is derived from all used runs,

$$A_{\text{eff}} = \sum_{all\ runs} w_{run} A_{eff}^{run}, \tag{5.3}$$

weighted with w_{run} due to the varying run livetime.

The run effective collection area A_{eff}^{run} takes the extension of the source region (here the inner 4° of the field of view) into account. The energy bin of the spectrum is divided into sub energy bins. The offset distribution of each sub energy bin is divided into offset bins. The optical efficiency o_{run} and the zenith angle z_{run} remain almost constant during one run. Thus the effective areas for all offset bins of the sub energy bins are weighted with the offset distribution to get an average effective area for the energy sub bin. The effective areas for the energy sub bins are then weighted with the energy distribution to get the effective collection area A_{eff}^{run} of one run:

$$A_{\text{eff}}^{run} = \sum_{E\ \epsilon\ \Delta E} w_E \Big(\sum_{\theta} w_\theta A_{\text{eff}}(E, z_{run}, \theta, o_{run})\Big) \tag{5.4}$$

with the weights w_E and w_θ derived from the offset and energy distribution in the sub-energy or energy bin, respectively.

It has to be kept in mind that this approach ignores the fact, that the effective areas are determined usually with simulations with power law index of 2 whereas the electron spectrum is known to be considerably steeper and this results in slightly different effective areas. This correction is rather be complicated, but has to be included in future.

5.4 Energy threshold

The energy threshold for spectral analysis depends both on the energy resolution and the effective area.

In [10] a "safe energy threshold" is determined by requiring, the relative energy bias $(E_{reco} - E_{true})/E_{true}$ below 10%. An other way to describe the energy bias is

$$bias = \log\left(\frac{E_{reco}}{E_{true}}\right). \tag{5.5}$$

Per definition the energy bias is equal to 0, if $E_{reco} = E_{true}$, analogously to the relative energy. 10% relative energy bias corresponds to a bias of 0.04 in the logarithmic definition. A negative bias stands for a too low reconstructed energy, whereas a positive value results from overestimated energies.

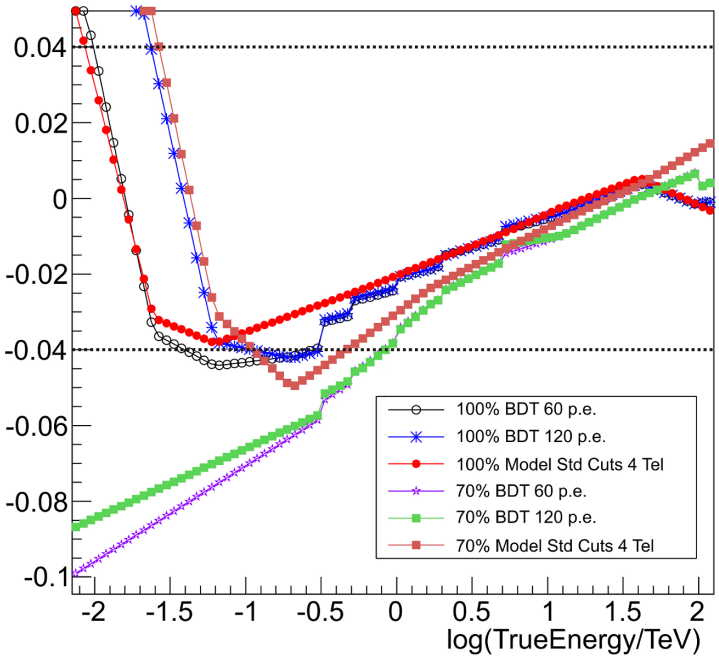

Figure 5.2: Energy bias, defined as $\log(E_{reco}/E_{true})$, for optical efficiencies of 70% and 100% at zenith angle 26° and at camera centre. A lower optical efficiency moves the secure energy threshold to larger energies.

Figure 5.2 shows the energy bias for the BDT analysis presented in this work with charge cuts of 60 p.e. and 120 p.e and the model standard cuts at a zenith angle of 26° at camera centre for two different optical efficiencies. The energy bias of BDT cuts and model standard cuts of the corresponding optical efficiency is almost equal above 300 GeV for 100% and respectively above

1 TeV for 70% optical efficiency, below this energy value of 300 GeV the model cuts provide a better energy reconstruction. The charge cut influences the energy bias only at low energies, above 300 GeV there are no differences between the BDT cut with a charge cut of 60 p.e. or 120 p.e. A reduced optical efficiency degrades the energy bias and shifts the secure energy threshold to higher energies. Again the BDT application in energy bins results in step-like features also in the energy bias.

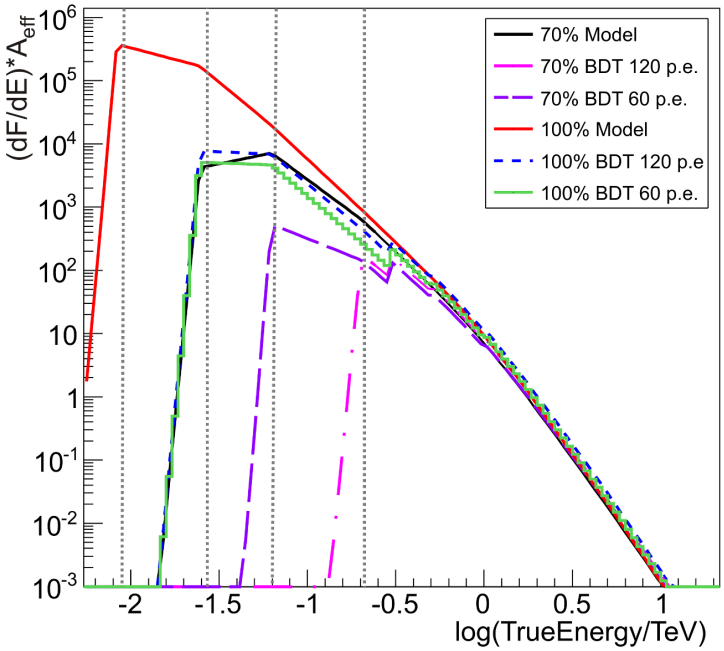

Figure 5.3: Differential γ-ray detection flux for optical efficiencies of 70% and 100% at a zenith angle of 26° and at camera centre. The flux dependent energy thresholds are indicated with grey dotted vertical lines.

An alternative definition of the energy threshold is based on the effective collection area and the expected flux of the observed source. It is defined as the peak in the differential γ-ray detection rate, that is derived by multiplication of the source's expected differential energy flux and the effective collection area [43]. The differential cosmic-ray electron flux measured by H.E.S.S. [4] was used for this estimation. The differential rate is illustrated in figure 5.3 for different cuts and optical efficiencies. The flux-dependent energy thresholds are indicated with grey dotted vertical lines. As expected the energy threshold moves to higher energies with worse optical efficiency. This results from the optical efficiency dependence of the effective areas. The lower energy thresholds of the model standard cuts are caused by the better effective areas below 300 GeV. The charge cut effects are stronger at lower optical efficiencies than at a perfect one.

In comparison the flux-dependent energy thresholds are lower than the secure energy threshold. There are no restrictions to a low-energy electron spectrum below 300 GeV from the effective areas, but the lower energy limit is strongly constrained by the energy bias. Thus for a electron analysis at low energies it is necessary to advance the energy bias of the BDT cuts and dataselection. But the energy bias with model standard cuts depends on the optical efficiency of the telescopes and at 70% optical efficiency the energy threshold is increased to almost 450 GeV. Hence, it is not only possible to derive an low energy threshold with better cuts and event selection, but also with strict constraints on the optical efficiency of the for analysis used observations.

Chapter 6

Study of an electron/γ-ray separation

There are several motivations for an attempt of a electron/γ-ray separation. Analysis of electron and γ-ray simulations shows at low energies differences between the shower evolution of electron and γ-ray initiated air showers [29], as already mentioned in Section 3.1. An advanced reconstruction technique [3], described in Section 4.1, provides the depth of first interaction as additional parameter to the depth of shower maximum. This parameter is sensitive to electron or γ-ray initiated air showers.

In Chapter 4 it was demonstrated that a satisfactory electron/hadron separation can be achieved. By using data from extragalactic fields one could avoid the galactic diffuse γ-ray background. However, an electron spectrum obtained from these selected data will still contain a certain contamination from the extragalactic diffuse γ-ray background which has not yet been measured in the H.E.S.S. energy range.

Section 6.1 gives an overview of existing measurements of the extragalactic γ-ray background in other energy regimes, while Section 6.2 shows the attempt of an electron/γ-ray separation with the BDT method.

6.1 Extragalactic diffuse γ-ray background

The high-energy diffuse γ-ray emission is composed of a galactic component, and a so-called extragalactic component, the *extragalactic γ-ray background* (EGRB). The galactic background is dominated by γ-rays produced by cosmic-ray interactions with interstellar gas and radiation fields. The much fainter extragalactic component was detected by the SAS-2 satellite [45] and later confirmed by the EGRET data [46]. The components that may make a contribution to the EGRB are unknown, but it is considered that the EGRB consists of a superposition of unresolved extragalactic sources including active galactic nuclei, starburst galaxies and γ-ray bursts as well as diffuse emitted radiation. These diffuse-emission processes could be potential signatures of large-scale structure formation, emission produced by the interaction of very high-energy cosmic rays with relic photons, annihilation and decay processes of dark matter and many more (see [47] and references therein).

The TeV flux of the EGRB is not known, only fluxes up to 10 GeV from the EGRET Analysis [46, 48] were measured in the last years. Recently the Fermi-LAT collaboration published the flux

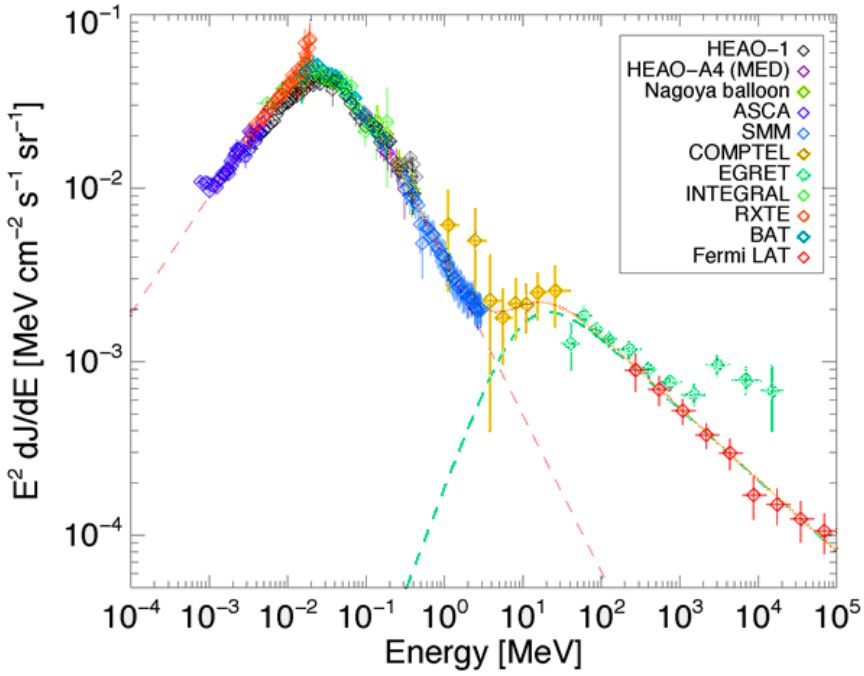

Figure 6.1: extragalactic diffuse high-energy background (taken from [44]). The measuremnts were recently extended by Fermi-LAT up to 100 GeV and the Fermi-LAT spectrum is significantly softer than the EGRET measurement.

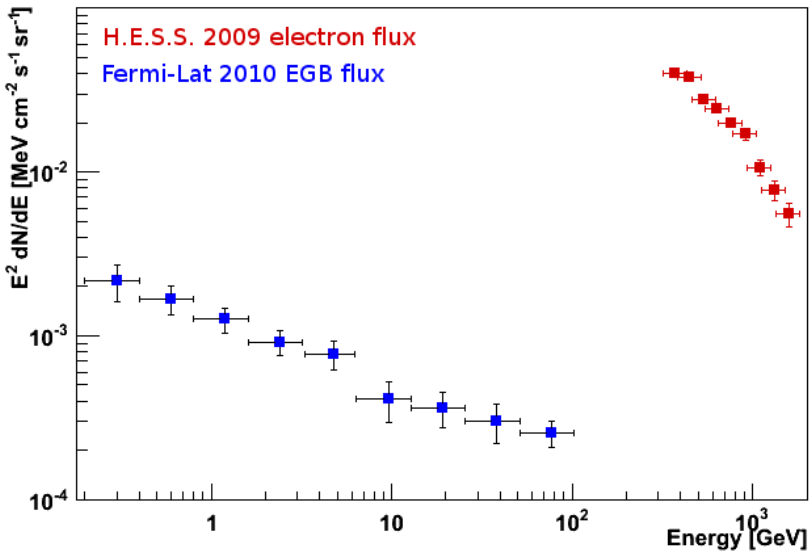

Figure 6.2: Comparison of the Fermi-LAT EGRB flux with H.E.S.S. electron flux, Fermi-LAT data taken from [47], H.E.S.S. from [4]. The extrapolated EGRB flux is more than one and a half orders of magnitude lower than the H.E.S.S. measured flux of high-energy cosmic-ray electrons.

of the EGRB above 200 MeV up to 100 GeV [47]. Figure 6.1 shows the extragalactic diffuse high-energy background with the new Fermi-LAT data. The Fermi-LAT spectrum can be described by a power law with index $\Gamma = 2.41 \pm 0.05$. It is significantly softer than the EGRET spectrum with a photon index $\Gamma = 2.13 \pm 0.03$. The authors of [47] argue, that this difference cannot be caused only by Fermi-LAT's better point source resolution as compared to EGRET.

Figure 6.2 shows the Fermi-LAT EGRB spectrum and the H.E.S.S. high-energy cosmic-ray electron spectrum. There is no measurement of the EGRB in the H.E.S.S. energy range available, but an extrapolation of the Fermi-LAT flux yields a flux almost two orders of magnitude less than the cosmic-ray electron flux measured by H.E.S.S. However an successful electron/γ-ray separation could quantify this.

6.2 BDT application to electrons and γ-rays

The used reconstruction technique (see Section 4.1) provides as shower parameter the depth of first interaction. Statistically electrons start to shower immediately when entering the atmosphere whereas photons start their air showers on average at a depth of $1\,X_0$. This was the motivation for testing the BDT method that was described in Chapter 4.2 on electron and γ-ray Monte Carlo simulations.

6.2.1 Training parameters and BDT settings

For the electron/γ separation the same training variables as for the electron/hadron separation were used (see section 4.3.3) also with the same bins in energy and zenith angle. Variations of the BDT settings did not improve the separation power, therefore the same settings were used.

Figure 6.3 shows the training input variables for energies between 5 TeV and 100 TeV and for zenith angle of 26°. The signal events are electron Monte Carlo simulations that were also used for electron/hadron separation. The background consists of events of γ Monte Carlo simulations with a power law spectrum with a photon index 2. Just like the electrons the γ-rays were simulated at fixed zenith angles 0°, 18° and 26°. The energy range is from 50 GeV to 100 TeV.

Obviously the training parameters for electrons and γ-rays are very similar, because both electrons and γ-rays induce electromagnetic air showers entering the Earth's atmosphere. Just a few parameters show slightly different distributions like for example the depth of first interaction and the depth of shower maximum.

6.2.2 Correlations and importance of the training parameters

Most training parameters are not or only slightly correlated, but the distributions of these variables are almost equal for electron- and γ-ray-induced air showers. Many correlations depend only marginally on the energy or zenith angles and remain almost constant, but a few show interesting trends. Figure 6.4 illustrates the energy dependence of the correlation coefficients between depth of first interaction and depth of shower maximum, depth of first interaction and Mean Scaled Length and also between depth of shower maximum and Mean Scaled Length for zenith. Their correlation coefficients and trends at 18° and 26° are very similar to the presented ones.

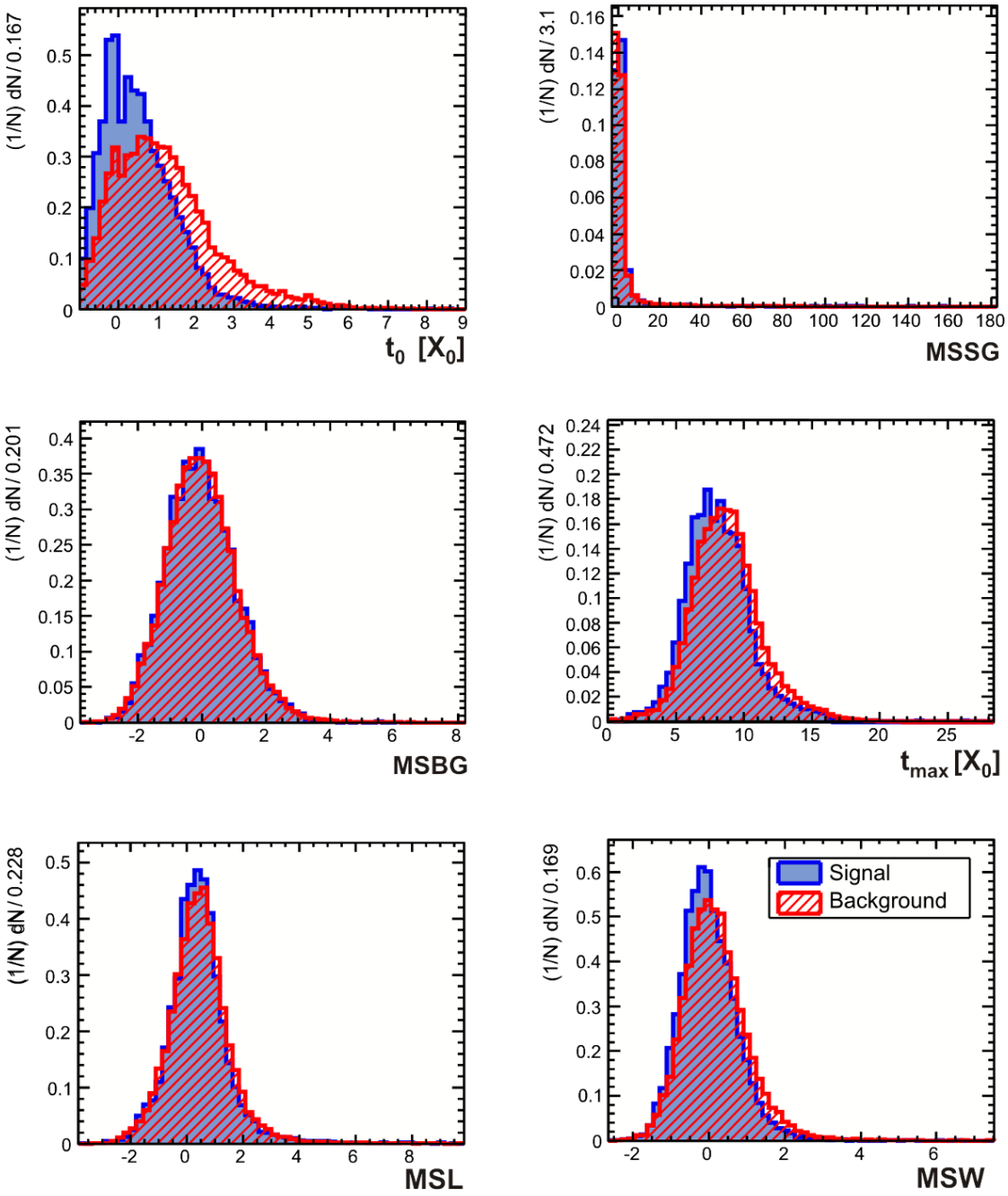

Figure 6.3: Training variables for electron/γ separation for energies between 5 TeV and 100 TeV and zenith angles between 22° and 30°.

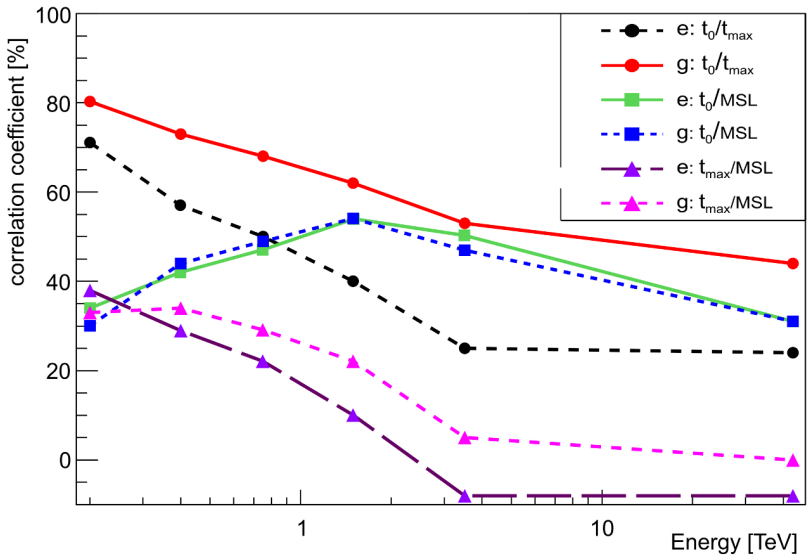

Figure 6.4: Various correlation coefficients for electron and photon showers as a function of shower energy at zenith angle 0°.

As expected, the depth of first interaction and depth of shower maximum have the largest correlation, but their correlation coefficient depends strongly on energy. At low energies they are correlated to 72 % for electrons and to 80 % for γ-rays. The correlations decrease with increasing energy and at high energies the correlations drop to 32 % and 52 %, respectively. The difference in the parameter correlations between electrons and γ-rays increases for higher energies.

The correlation coefficients of electron and γ-ray induced air showers do not differ this much for all other correlations between the training parameters. Figure 6.4 also shows the trend of the correlation coefficients between the depth of first interaction and the Mean Scaled Length. Here both correlation coefficients have the same trend and the differences are very small. There is no plausible explanation at the moment and these correlations should be checked with a different BDT implementation and another multivariate algorithm to exclude dependencies to the BDT implementation of the TMVA toolkit and test if this is really a hint at the different shower evolution.

The importance ranking of the training parameters is shown in figure 6.5. For definition of importance see Section 4.3.4. The most important parameter is the depth of first interaction followed by the depth of shower maximum. The remaining parameters have an importance less than 10% and do not contribute much for a possible electron/γ separation.

6.2.3 BDT response for electrons and γ-rays

An example of a BDT output distribution for energies between 5.0 TeV and 100 TeV and zenith angles between 22° and 30° is shown in figure 6.6 (for the BDT response of all energy and zenith angle bins see Appendix B). In contrast to the BDT output distribution for electron/hadron separation (see figure 4.7 Section 4.3.5) no clear separation between signal and background with a simple cut on the BDT response is possible for the electron/γ discrimination. There is only a small difference in the position of the response maximum for signal and background, so there is no basis for an event classification of electron and γ-ray events which could provide a good background rejection.

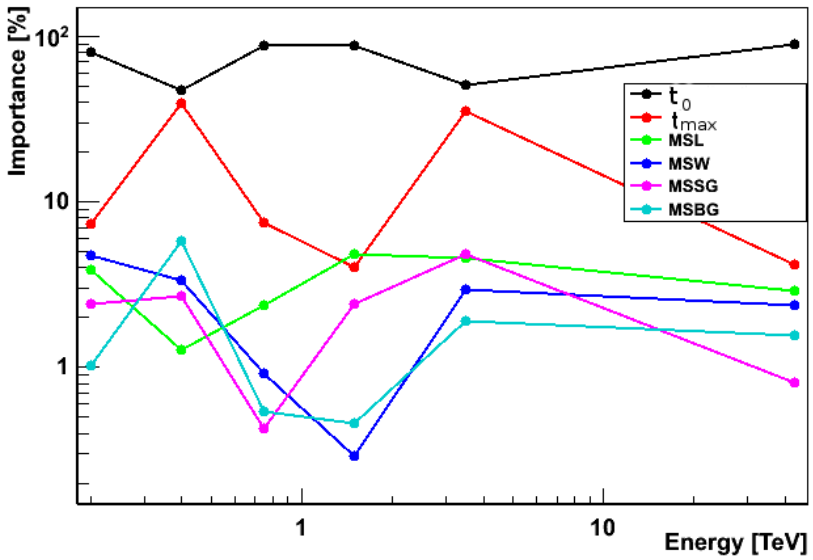

Figure 6.5: Importance ranking of training parameters for electron/γ separation at zenith angle 0°

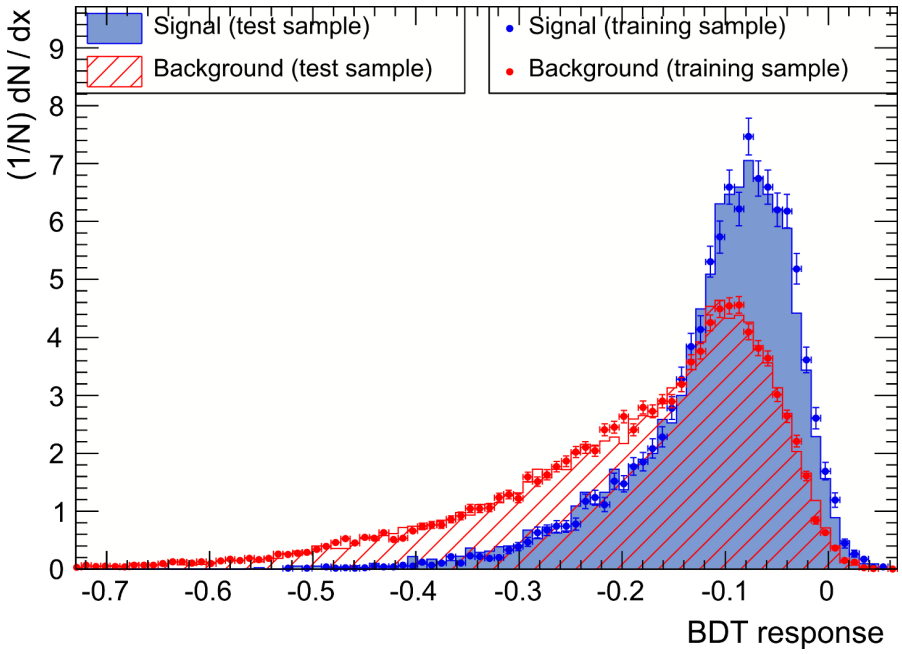

Figure 6.6: Distribution of the BDT response for energies between 5.0 TeV and 100 TeV and a zenith angles between 22° and 30°. Signal refers to electrons and background to γ-rays from Monte Carlo simulations.

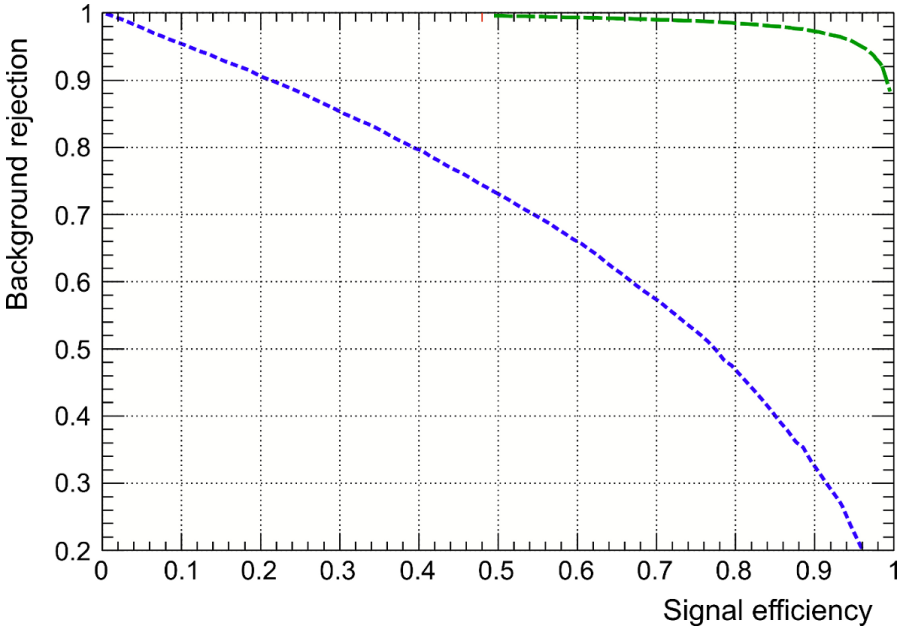

Figure 6.7: Signal efficiency vs background rejection for energies between 5 and 100 TeV and zenith angles between 22° and 30° for electron/γ-rays (blue) and electron/hadrons (green).

This result is also clearly illustrated in figure 6.7, where the signal efficiency versus the background rejection for energies between 5 TeV and 100 TeV and zenith angles between 22° and 30° is shown. The signal versus background rejection curve for the attempt of electron/γ-ray separation is illustrated in blue, where as this curve for the hadron/electron separation is coloured in green. The separation between electrons and hadrons can be achieved with good signal efficiencies, where as a a electron/γ-ray separation with good signal efficiency and background rejection is with the strategy here applied not feasible.

Even using another multivariate algorithm seems not promising, because the signal and background distributions of the shower variables are too small in the analysed energy and zenith angle bin. This study was limited to small zenith angles between 0° and 30°, thus not the whole zenith range was studied. H.E.S.S. is going to be extended with an fifth telescope, that provides a larger reflector area than the four other telescopes and decreases the energy threshold. Thus, an examination at lower energies is possible.

Chapter 7

Conclusion and outlook

This work started with an overview of high-energy cosmic-ray electrons and the H.E.S.S. experiment. The energy spectrum of cosmic-ray electrons has already been measured with the H.E.S.S. experiment, using the standard Hillas reconstruction technique. An advanced γ-ray reconstruction method (model analysis), developed as alternative reconstruction technique to the standard Hillas reconstruction technique, is more sensitive to electromagnetic air showers.

The aim of this work was to study the electron reconstruction with the model analysis. Although it was not possible to present a differential energy spectrum of high-energy cosmic-ray electrons in this work, the basic steps necessary to obtain the spectrum are described in detail.

The electron identification is carried out with electron/hadron separation using the Boosted Decision Tree method from the TMVA-Toolkit. This separation can be easily achieved with the selected shower parameters and it shows good signal efficiencies.

One important part in the determination of the differential energy spectrum is the effective collection area, that is directly affected by data selection and electron/hadron separation cuts. Various dependencies of the effective areas are discussed. In most parts of the energy range the effective area, using the BDT response cut, is comparable or larger than the effective area determined with model standard cuts. A flux-dependent energy threshold of below 100 GeV also for optical efficiencies smaller than 100% was determined for a charge cut of 60 p.e. But the energy threshold also depends on the energy resolution and energy bias. Here the event selection and BDT cut lead to a higher energy bias than with model standard cuts.

The determination of the differential energy spectrum of high-energy cosmic-ray electrons, using the model analysis as reconstruction technique and the BDT method for electron/hadron separation, works very well for energies above 500 GeV also with optical efficiencies less than 100%, but for a low-energy analysis, where a better energy bias is needed, the data selection and BDT cut have to be improved.

The use of the model analysis for reconstruction instead of the Hillas standard reconstruction provides the depth of first interaction as additional shower parameter besides the depth of shower maximum; both parameters that are sensitive to the differences between electron and γ-ray initiated air showers. This motivated a study of electron/γ-ray separation with the BDT method. But a electron/γ-ray discrimination on a event-by-event basis with good signal efficiencies is not possible to achieve with the strategy applied here.

The electron/γ-ray separation was only analysed in the zenith angle range between 0° and 30°, but there are only small chances to get at higher zenith angles better results with the BDT

method. Other multivariate methods do also not seem promising because the shower parameters provided by the Hillas standard reconstruction and model analysis are too similar for electron and γ-ray induced air showers. Thus, a possible approach could be to find other shower parameters, that differ more for electron and γ-ray initiated air showers. The H.E.S.S. extension with an fifth telescope decreases the energy threshold, which allows an analysis below 100 GeV.

Appendix A

BDT response for electron/hadron separation

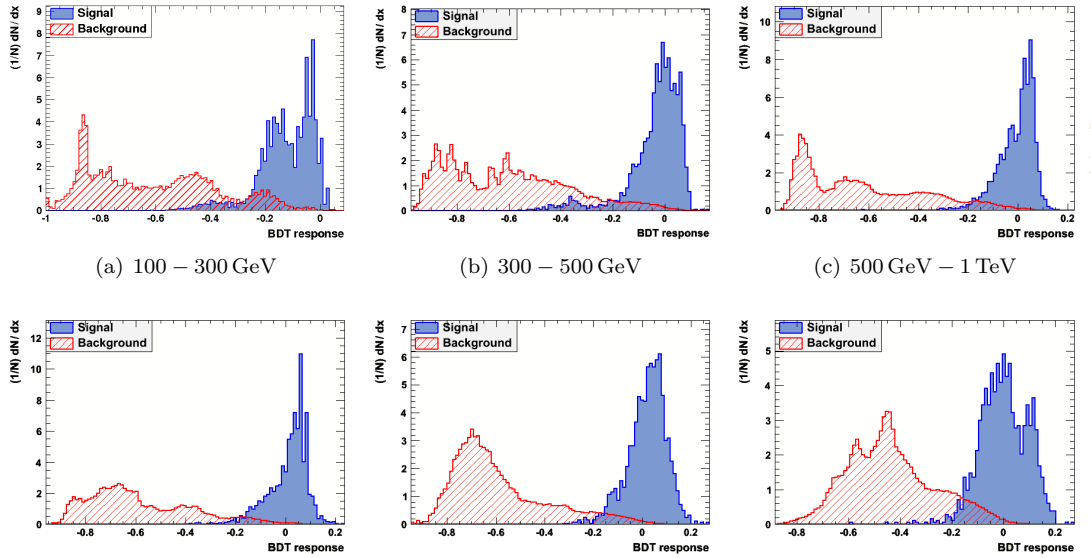

(a) $100 - 300\,\mathrm{GeV}$ (b) $300 - 500\,\mathrm{GeV}$ (c) $500\,\mathrm{GeV} - 1\,\mathrm{TeV}$

(d) $1 - 2\,\mathrm{TeV}$ (e) $2 - 5\,\mathrm{TeV}$ (f) $5 - 100\,\mathrm{TeV}$

Figure A.1: BDT response for electron/hadron separation for all energy bins at zenith.

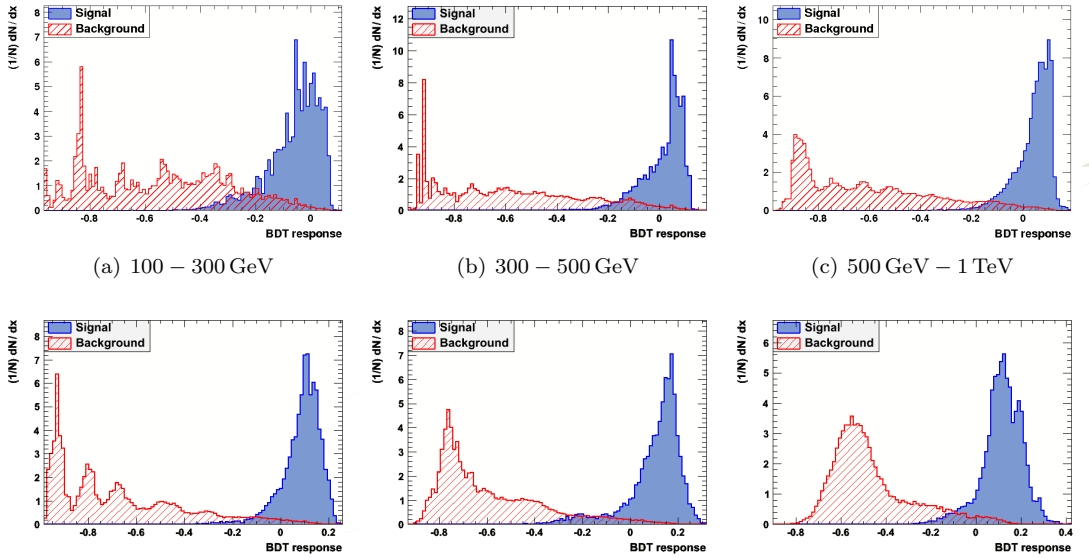

(a) 100 – 300 GeV (b) 300 – 500 GeV (c) 500 GeV – 1 TeV

(d) 1 – 2 TeV (e) 2 – 5 TeV (f) 5 – 100 TeV

Figure A.2: BDT response for electron/hadron separation for all energy bins at a zenith angle of 18°.

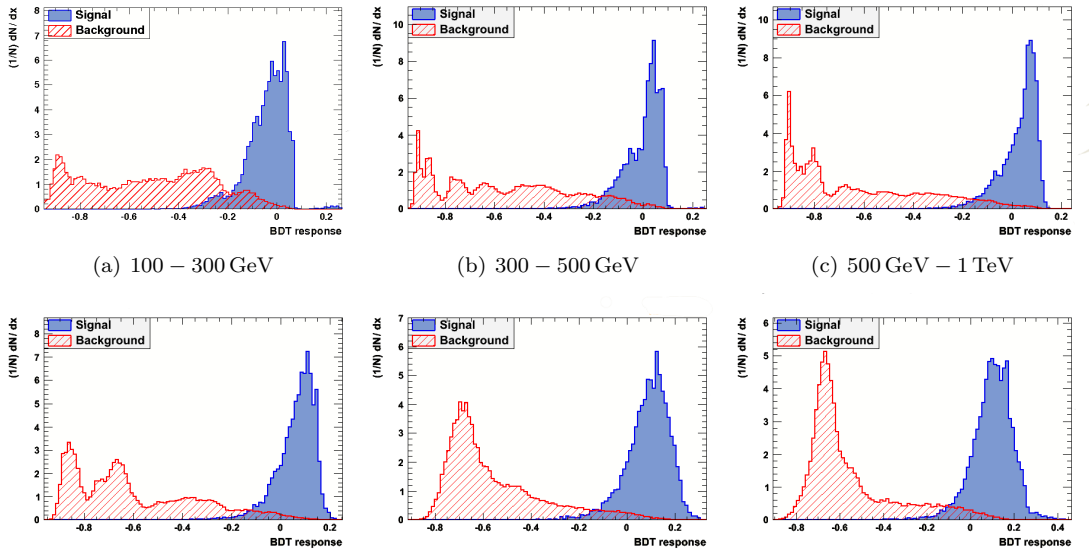

(a) 100 – 300 GeV (b) 300 – 500 GeV (c) 500 GeV – 1 TeV

(d) 1 – 2 TeV (e) 2 – 5 TeV (f) 5 – 100 TeV

Figure A.3: BDT response for electron/hadron separation for all energy bins at a zenith angle of 26°.

Appendix B

BDT response for electron/γ-ray separation

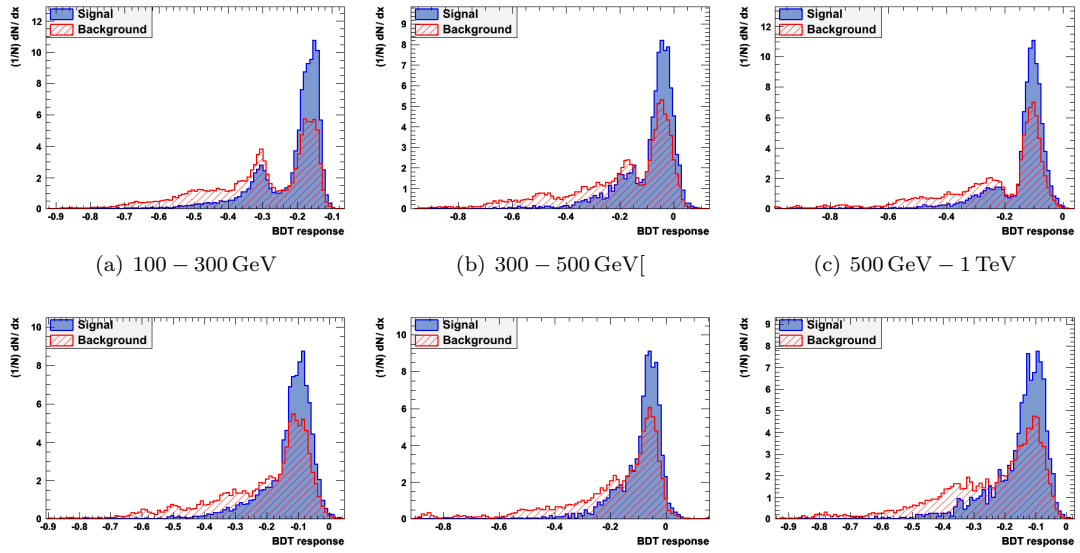

(a) $100 - 300\,\mathrm{GeV}$ (b) $300 - 500\,\mathrm{GeV}[$ (c) $500\,\mathrm{GeV} - 1\,\mathrm{TeV}$

(d) $1 - 2\,\mathrm{TeV}$ (e) $2 - 5\,\mathrm{TeV}$ (f) $5 - 100\,\mathrm{TeV}$

Figure B.1: BDT response for electron/γ-ray separation for all energy bins at zenith.

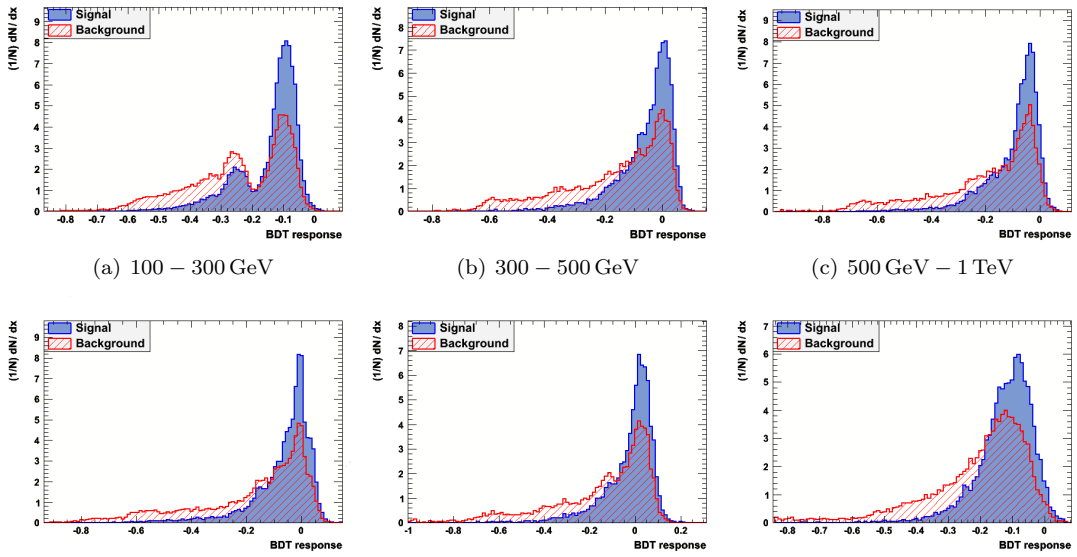

(a) $100 - 300\,\mathrm{GeV}$ (b) $300 - 500\,\mathrm{GeV}$ (c) $500\,\mathrm{GeV} - 1\,\mathrm{TeV}$

(d) $1 - 2\,\mathrm{TeV}$ (e) $2 - 5\,\mathrm{TeV}$ (f) $5 - 100\,\mathrm{TeV}$

Figure B.2: BDT response for electron/γ-ray separation for all energy bins at a zenith angle of 18°.

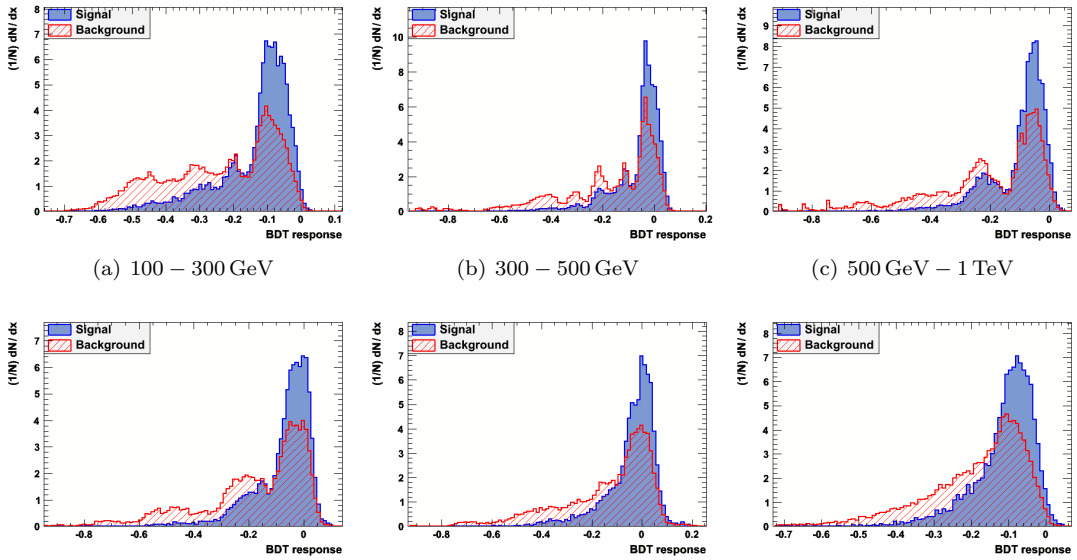

(a) $100 - 300\,\mathrm{GeV}$ (b) $300 - 500\,\mathrm{GeV}$ (c) $500\,\mathrm{GeV} - 1\,\mathrm{TeV}$

(d) $1 - 2\,\mathrm{TeV}$ (e) $2 - 5\,\mathrm{TeV}$ (f) $5 - 100\,\mathrm{TeV}$

Figure B.3: BDT response for electron/γ-ray separation for all energy bins at a zenith angle of 26°.

Bibliography

[1] F. Aharonian et al. The energy spectrum of cosmic-ray electrons at TeV energies. *Phys. Rev. Lett.*, 101:261104, 2008.

[2] HESS Collaboration: F. Acero et al. First detection of VHE gamma-rays from SN 1006 by H.E.S.S. *ArXiv e-prints*, 1004.2124, 2010.

[3] M. de Naurois and L. Rolland. A stereoscopic semi-analytical model reconstruction of gamma-rays for Imaging Atmospheric Cherenkov Telescopes. *Astropart. Phys.*, 32:231, 2009.

[4] F. Aharonian et al. Probing the ATIC peak in the cosmic-ray electron spectrum with H.E.S.S. *Astron. Astrophys.*, 508:561, 2009.

[5] J. Chang et al. An excess of cosmic ray electrons at energies of 300-800 GeV. *Nature*, 456:362–365, 2008.

[6] S. Torii et al. High-energy electron observations by PPB-BETS flight in Antarctica. *ArXiv e-prints*, 0809.0760, 2008.

[7] T. Kobayashi, Y. Komori, K. Yoshida, and J. Nishimura. The Most Likely Sources of High Energy Cosmic-Ray Electrons in Supernova Remnants. *Astrophys. J.*, 601:340–351, 2004.

[8] A. A. Abdo et al. Measurement of the Cosmic Ray $e^+ + e^-$ Spectrum from 20 GeV to 1 TeV with the Fermi Large Area Telescope. *Phys. Rev. Lett.*, 102(18):181101, 2009.

[9] D. Malyshev, I. Cholis, and J. Gelfand. Pulsars versus Dark Matter Interpretation of ATIC/PAMELA. *Phys. Rev D.*, 80:063005, 2009.

[10] F. Aharonian et al. Observations of the Crab Nebula with H.E.S.S. *Astron. Astrophys.*, 457:899–915, 2006.

[11] M. Longair. *High Energy Astrophysics Vol. II.* Cambridge University Press, second edition, 1994.

[12] O. C. de Jager and A. Djannati-Ataï. Implications of H.E.S.S. observations of pulsar wind nebulae. *ArXiv e-prints*, 0803.0116, 2008.

[13] T. Delahaye, J. Lavalle, R. Lineros, F. Donato, and N. Fornengo. Galactic electrons and positrons at the Earth: new estimate of the primary and secondary fluxes. *ArXiv e-prints*, 1002.1910, 2010.

[14] K. Egberts. *The Energy Spectrum of Cosmic-Ray Electrons Measured with H.E.S.S.* PhD thesis, Ruprecht-Karls-Universität Heidelberg, 2008.

[15] C. S. Shen and C. Y. Mao. Anisotropy of High Energy Cosmic-Ray Electrons in the Discrete Source Model. *Astrophys. Lett.*, 9:169, 1971.

[16] V. S. Ptuskin and J. F. Ormes. Expected Anisotropy of Very High Energy Electrons. In *International Cosmic Ray Conference*, volume 3, page 56, 1995.

[17] L. O'C. Drury. An introduction to the theory of diffusive shock acceleration of energetic particles in tenuous plasmas. *Rep. Prog. Phys.*, 46:973–1027, 1983.

[18] E. Fermi. On the Origin of the Cosmic Radiation. *Phys. Rev.*, 75:1169–1174, 1949.

[19] W. I. Axford, E. Leer, and G. Skadron. The Acceleration of Cosmic Rays by Shock Waves. In *International Cosmic Ray Conference*, volume 11, page 132, 1977.

[20] G. F. Krymskii. A regular mechanism for accelerating charged particles at the shock front. *Akademiia Nauk SSSR Doklady*, 234:1306–1308, 1977.

[21] A. R. Bell. The acceleration of cosmic rays in shock fronts. I. *Monthly Notices of the Royal Astronomical Society*, 1822:147–156, 1978.

[22] R. D. Blandford and J. P. Ostriker. Particle Acceleration by Astrophysical Shocks. *Astrophys. J.*, 221:L29–L32, 1978.

[23] W. Heitler. *Quantum Theory of Radiation*. Dover Press, third edition, 1954.

[24] C. Amsler and others (Particle Data Group). Review of particle physics. *Phys. Lett. B*, 667:1, 2008.

[25] M. Longair. *High Energy Astrophysics Vol. I.* Cambridge University Press, second edition, 1992.

[26] F. Aharonian, J. Buckley, T. Kifune, and G. Sinnis. High energy astrophysics with ground-based gamma ray detectors. *Rep. Prog. Phys*, 71:096901, 2008.

[27] H. J. Voelk and K. Bernloehr. Imaging Very High Energy Gamma-Ray Telescopes. *Exper. Astron.*, 25:173–191, 2009.

[28] B. Rossi. *High-Energy Particles*. Prentice-Hall, New York, 1952.

[29] V. Sahakian, F. Aharonian, and A. Akhperjanian. Cherenkov light in electron-induced air showers. *Astropart. Phys.*, 25:233–241, 2006.

[30] J. Davies and E. Cotton. *Journal of Solar Energy*, 1:16, 1957.

[31] K. Bernloehr et al. The optical system of the H.E.S.S. imaging atmospheric Cherenkov telescopes, Part I: layout and components of the system. *Astropart. Phys.*, 20:111–128, 2003.

[32] R. Cornils et al. The optical system of the H.E.S.S. imaging atmospheric Cherenkov telescopes, Part II: mirror alignment and point spread function. *Astropart. Phys.*, 20:129–143, 2003.

[33] S. Funk et al. The trigger system of the H.E.S.S. telescope array. *Astropart. Phys.*, 22:285–296, 2004.

[34] F. Aharonian et al. Calibration of cameras of the H.E.S.S. detector. *Astropart. Phys.*, 22:109–125, 2004.

[35] A. M. Hillas. Cerenkov light images of EAS produced by primary gamma. In F. C. Jones, editor, *International Cosmic Ray Conference*, volume 3, pages 445–448, 1985.

[36] S. Bolz. *Absolute Energiekalibration der abbildenden Cherenkov-Teleskope des H.E.S.S. Experiments und Ergebnisse erster Beobachtungen des Supernova-Überrests RX J1713.7-3946.* PhD thesis, Ruprecht-Karls-Universität Heidelberg, 2004.

[37] S. Ohm, Ch. van Eldik, and K. Egberts. Gamma-Hadron Separation in Very-High-Energy gamma-ray astronomy using a multivariate analysis method. *Astropart. Phys.*, 31:383–391, 2009.

[38] A. Fiasson, F. Dubois, G. Lamanna, J. Masbou, and S. Rosier-Lees. Optimization of multivariate analysis for IACT stereoscopic systems. *ArXiv e-prints*, 1004.3375, 2010.

[39] D. Berge, S. Funk, and J. Hinton. Background Modelling in Very-High-Energy gamma-ray Astronomy. *Astron. Astrophys.*, 466:1219–1229, 2007.

[40] A. Hoecker, J. Stelzer, and F. Tegenfeldt. *Toolkit for Multivariate Data Analysis with ROOT - Users Guide*, 2007.

[41] M. P. Ketzman and G. H. Sembroski. *Nucl. Instrum. Meth. A*, 347:629–643, 1994.

[42] M. de Naurois. H.E.S.S internal documentation.

[43] A. Konopelko et al. Performance of the Stereoscopic System of the HEGRA Imaging Air Cerenkov Telescopes: Monte Carlos Simulations & Observations. *Astropart. Phys.*, 10:275, 1999.

[44] U. Oberlack. Extragalactic diffuse gamma-ray emission at high energies. *Physics 3*, 21, 2010.

[45] D. J. Thompson and C. E. Fichtel. Extragalactic gamma radiation - Use of galaxy counts as a galactic tracer. *Astron. Astrophys.*, 109:352–354, 1982.

[46] P. Sreekumar et al. EGRET Observations of the Extragalactic Gamma-Ray Emission. *Astrophys. J.*, 494:523, 1998.

[47] A. A. Abdo et al. Spectrum of the Isotropic Diffuse Gamma-Ray Emission Derived from First-Year Fermi Large Area Telescope Data. *Phys. Rev. Lett.*, 104(10):101101, 2010.

[48] A. W. Strong, I. V. Moskalenko, and O. Reimer. A New Determination of the Extragalactic Diffuse Gamma-Ray Background from EGRET Data. *Astrophys. J.*, 613:956–961, 2004.

Danksagung

Das letzte Jahr, das ich mit meiner Diplomarbeit verbracht habe, war ein sehr lehreiches, aber auch anstrengendes Jahr. Ich möchte mich bei allen bedanken, die mich unterstützt haben oder an dieser Arbeit beteiligt waren.
Insbesondere möchte ich mich bedanken bei:

meinen Eltern und meinem Freund, für die Unterstützung und den Rückhalt während des gesamten Studiums und auch die ganzen Jahre davor.

Herrn Prof. Christian Stegmann, für die Möglichkeit diese Themenstellung zu bearbeiten, seine ansteckende Begeisterung und für die Teilnahme am Spiegelaustausch in Namibia.

Dr. Kathrin Valerius, für die Betreuung meiner Arbeit, ihre Hifsbereitschaft, die immer offene Tür und die Zeit, die sie sich für mich immer genommen hat. Außerdem noch vielen Dank für das ausfühliche Korrekturlesen dieser Arbeit.

Dr. Ira Jung, für ihre Hilfsbereitschaft und das ausführliche Beantworten meiner Fragen zur Kallibration, Standard-Hillas-Rekonstruktion und DST-Konvertierung.

Dr. Mathieu de Naurois, für die Monte-Carlo-Simluationen und die vielen, jeweils in kürzester Zeit beantworteten Fragen.

Dr. Kathrin Egberts, für die Woche in Erlangen, in der ich sehr viel Einblicke in das Erstellen eines Elektronenspektrums gewonnen habe.

Fabian Schöck, für das Korrekturlesen dieser Arbeit und seine Anmerkungen.

Bernhard Glück, für das detailierte Beantworten meiner Fragen von Triggerraten bis zu Teleskop-koordinatensystemen.

der gesammten H.E.S.S. Gruppe Erlangen, für die angenehme Atmosphäre und Hilfsbereitschaft.

Erklärung

Hiermit bestätige ich, dass ich diese Arbeit selbstständig und nur unter Verwendung der angegebenen Hilfsmittel angefertigt habe.

Erlangen,

Stephanie Häffner